Seventh International Conference on Computational Fluid Dynamics (ICCFD7), Big Island, Hawaii, July 9-13, 2012

ICCFD7-3506

Advances in Rotor Performance and Turbulent Wake Simulation using DES and Adaptive Mesh Refinement

Neal M. Chaderjian[*]
Corresponding author: Neal.Chaderjian@nasa.gov

[*]NASA Ames Research Center, Moffett Field, CA, USA

Abstract: Time-dependent Navier-Stokes simulations have been carried out for a rigid V22 rotor in hover, and a flexible UH-60A rotor in forward flight. Emphasis is placed on understanding and characterizing the effects of high-order spatial differencing, grid resolution, and Spalart-Allmaras (SA) detached eddy simulation (DES) in predicting the rotor figure of merit (FM) and resolving the turbulent rotor wake. The FM was accurately predicted within experimental error using SA-DES. Moreover, a new adaptive mesh refinement (AMR) procedure revealed a complex and more realistic turbulent rotor wake, including the formation of turbulent structures resembling vortical worms. Time-dependent flow visualization played a crucial role in understanding the physical mechanisms involved in these complex viscous flows. The predicted vortex core growth with wake age was in good agreement with experiment. High-resolution wakes for the UH-60A in forward flight exhibited complex turbulent interactions and turbulent worms, similar to the V22. The normal force and pitching moment coefficients were in good agreement with flight-test data.

Keywords: Higher-order differences, adaptive mesh refinement, detached eddy simulation, figure of merit.

1. Introduction

Rotorcraft perform many useful civil and military functions by virtue of their ability to take off and land vertically. Two examples of rotary wing designs are shown in Fig. 1. Modern designs continue to push the technology to improve vehicle performance, safety, and reduce its impact on the environment. However, the accurate simulation of rotorcraft flow fields with computational fluid dynamics (CFD) continues to be a challenging problem. Unlike fixed-wing applications, a rotor blade can encounter the tip vortices of other blades (Fig. 1a). This interaction can strongly affect the rotor blade loads and performance, and generate high levels of noise and vibration. The situation is further complicated by flexible rotor blades (Fig. 1b). Rotorcraft simulation is by nature time-dependent and multi-disciplinary, combining CFD with computational structural dynamics (CSD). Moreover, static flight requires a trim algorithm to ensure the prescribed thrust is acquired with zero pitch and roll moments.

For more than a decade, the accurate prediction of figure of merit (FM) has eluded CFD simulation of rotors in hover using the Navier-Stokes equations. The FM is defined as

$$\text{FM} = \frac{C_T^{3/2}}{\sqrt{2}C_Q} \tag{1}$$

where C_T is the thrust coefficient and C_Q is the torque coefficient. This expression is the ratio of the ideal torque (from momentum theory) to the actual torque. The FM can be viewed as a measure of the rotor blade efficiency, where CFD typically under-predicts experiment by 2-6%, depending on the thrust coefficient and numerical method. To bring this into perspective, every 0.5% error in FM corresponds to one less passenger, where a helicopter typically carries 2-6 passengers.


a) Bell-Boeing V-22 Osprey tiltrotor. b) Sikorsky UH-60 Blackhawk helicopter.

Figure 1 Two examples of rotary wing aircraft.

This shortcoming has been attributed to poor resolution of the rotor vortices. This is illustrated in Fig. 2 by the Navier-Stokes simulation of the V22 rotor in hover by Holst and Pulliam [1]. They utilize the OVERFLOW CFD code [2-3] to solve the steady Navier-Stokes equations in a non-inertial frame using 3rd-order spatial accuracy and the Spalart-Allmaras [4] one-equation turbulence model. Figure 2a uses a wake grid spacing of Δ=10%c_{tip} (blade tip chord), which is a common CFD practice, and is the approximate size of the physical vortex core diameter. The tip vortices are rendered using an iso-surface of vorticity. Note how quickly the vortices dissipate and the large size of the vortex cores, even though the inviscid Euler equations were solved in the wake region to reduce vortex diffusion. The computed FM=0.73 differs substantially from the experimental value of 0.78. Figure 2b shows a solution where the blade grids have twice the spatial resolution in all three directions than in Fig. 2a, and the wake grid spacing is Δ=1.25%c_{tip}. Note the vortices persist for a longer wake age, and the FM=0.77 is a significant improvement. An adaptive mesh refinement (AMR) procedure was used external to OVERFLOW in a loosely coupled manner to obtain the AMR mesh, which had 448 million grid points. Uniform grid refinement in the wake would have been computationally costly, resulting in several billion grid points.

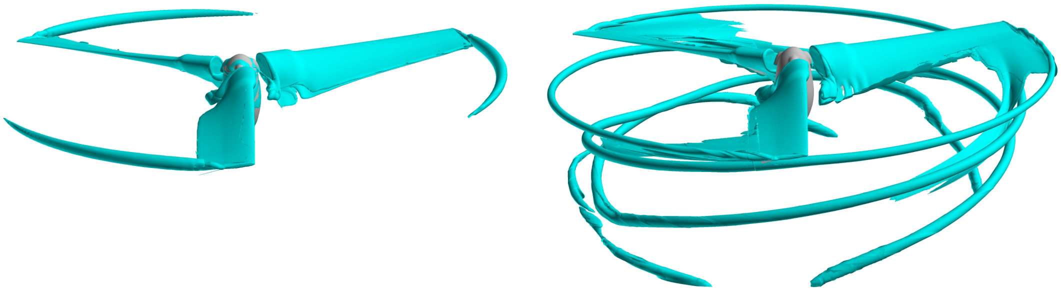
a) Baseline wake grid: Δ=10% c_{tip}., FM=0.73. b) AMR wake grid: Δ=1.25% c_{tip}, FM=0.77.

Figure 2 OVERFLOW simulation [1] of the V22 tiltrotor in hover, M_{tip}=0.625, θ=14°, Re=2.1 million.

Results such as those shown in Fig. 2 have led to a great deal of interest in resolving the rotor wake to a greater degree using automated AMR. However, Chaderjian and Buning [5] recently showed that high-resolution rotor wakes have little to do with the accurate prediction of FM. Moreover, their use of a new dynamic AMR procedure in OVERFLOW to highly resolve the rotor wake revealed a complex turbulent wake that included turbulent structures that resembled vortical worms. This paper will discuss the V22 results reported in Ref. [5] in greater depth, including additional supporting computations and analysis describing the numerical and physical mechanisms involved. Some additional results by Chaderjian and Ahmad [6] for the UH-60A flexible rotor in forward flight will also be included.

The following sections include a discussion of the experimental data, numerical approach, results and discussion, and concluding remarks.

2. Experimental Data

The numerical results presented in this paper are validated with wind-tunnel measurements and flight-test data. These experimental results are now briefly described.

The Tilt Rotor Aeroacoustics Model (TRAM) is a ¼-scale wind-tunnel model of the V22 Osprey rotor. This model was constructed and tested to facilitate tiltrotor aeromechanics research, and provides a significant source of aeroacoustic, performance, and structural loads data for validation of tiltrotor analyses. The stiff rotor blades are ideally suited for aerodynamic CFD validation without the additional uncertainty introduced by blade flexibility. The TRAM rotor was tested in the Duits-Nederlandse Windtunnel Large Low-speed Facility (DNW-LLF) in the spring of 1998. Table 1 summarizes the TRAM model geometric characteristics and nominal hover test conditions. A photo of the model is shown in Fig. 3 (airplane mode). The best hover data was obtained with the wind tunnel turned off and the rotor in "airplane" mode. This avoids the interaction of the rotor vortices with the tunnel floor. Further details about the TRAM wind-tunnel test can be found in Refs. [7-8].

Rotor Radius, R	57 inches
Solidity, σ	0.105
Tip Chord, c_{tip}	5.5 inches
Blade Twist	32° to -6°, nonlinear
Reynold's Number, Re	2.1 million
Tip Mach Number, M_{tip}	0.58, 0.62
Thrust Coefficient, C_T/σ	0.05-0.17
Collective Pitch Angle, θ	3° to 17°
FM Experimental Error	≈ ±0.005

Table 1 TRAM geometric characteristics and nominal hover test conditions.

Figure 3 TRAM model in airplane mode at the DNW wind tunnel.

NASA and the US Army, as a part of the UH-60A Airloads program, maintain an extensive flight-test database [9] for the Blackhawk helicopter (see Fig. 1b) in level flight and transient maneuvers. The database provides aerodynamic pressures, structural loads, control positions, and rotor forces and moments. Moreover, UH-60A rotor measurements at the United Technologies Research Center (UTRC) wind tunnel [10] provides experimental data that includes wake trajectory, blade loading, blade deformations, and performance measurements. The flight-test data is used to validate numerical simulations of the UH-60A rotor in forward flight.

3. Numerical Approach

The V22 rotor blades are shorter and stiffer than a typical helicopter rotor. Their design is dictated by the need to function both as a propeller (airplane mode) and as a rotor (helicopter mode). They can therefore be treated as rigid, and are ideally suited for assessment of numerical aerodynamic accuracy. On the other hand, the UH-60 rotor blades are much longer and more slender because flexibility is required due to material constraints and stress relief requirements.

The OVERFLOW CFD code is used to solve the time-dependent Navier-Stokes equations for isolated rotor flows in hover and forward flight. This CFD code has a variety of implicit and relaxation algorithms that utilize upwind and central spatial differencing. Both single and dual time integration options are available. Curvilinear and Cartesian overset grids are used to treat complex geometries and the surrounding flow domain. A variety of zero, one, and two-equation turbulence models are available to solve the Reynolds-averaged Navier-Stokes (RANS) equations. For more complex flows, transition trip lines and models, and detached eddy simulation (DES) are useful options. A more complete description of the OVERFLOW CFD code and its user's manual can be found in Refs. [2-3]. Some of the key aspects used in the present computations are described below.

3.1 Overset Grids

OVERFLOW solves the Navier-Stokes equations on structured overset grids. The current time-accurate approach consists of an inertial coordinate system where body-conforming O-grids rotate through a fixed Cartesian grid system. Figure 4 shows the rotor near-body (NB) O-grids that are used to resolve the flow in the vicinity of the rotor blades and simplified spinner/nacelle.

An off-body (OB) Cartesian grid system shown in Fig. 5 is designed to resolve the off-body vortex wake and extend the computational domain to the far field. Baseline solutions are obtained by using a uniform grid spacing (Δ=10%c_{tip}) on the first set of Level one (L1) grids. Additional "brick grids" are added to the L1 grids to rapidly extend the computational domain to the far field, which for the present computations is 17 rotor radii (R) from the blades. These brick grids are referred to as Levels 2, 3, …, each of which is a factor of 2 coarser in every direction than the previous grid level.

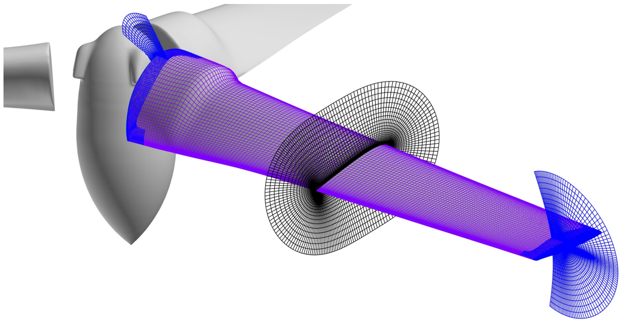

Figure 4 TRAM NB curvilinear O-grids.

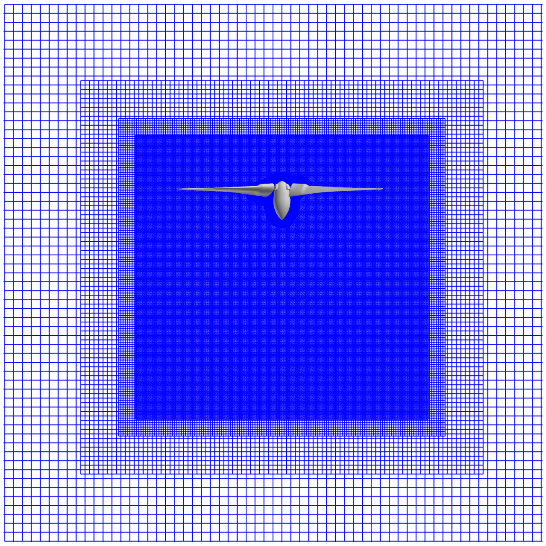

Figure 5 TRAM OB Cartesian grids.

Each rotor blade grid consists of a main-body O-mesh, and two O-mesh cap grids at the root and tip locations (see Fig. 4). The main rotor blade O-mesh consists of 181x175x66 grid points in the chordwise, radial, and body-normal directions. The average y-plus one point off of the blade surface is $y^+ \approx 0.2$. Details of the surface grid spacing and number of grid points are summarized in Tables 2-3. The L1 wake-grids extend 1.25R in the radial direction, 0.4R above the rotor blades, and 2.0R below the rotor blades. This baseline grid system consists of 35 million grid points. This is perhaps larger than is required to accurately predict FM, especially the location of the lower L1-grid boundary. However, these boundaries were chosen to reduce any chance that the wake-grid boundaries might influence the results. In practice, extending the L1 grid down about 1.0R would probably be sufficient. In this case, the total number of grid points would be about 25 million grid points.

$\Delta r/c_{tip}$	$\Delta c/c_{tip}$	$\Delta c_{LE}/c_{tip}$	$\Delta c_{TE}/c_{tip}$	No. TE Grid Cells
0.36%	1.56%	0.12%	0.03%	10

Table 2 Average TRAM rotor grid spacing in the radial and chordwise directions near the outboard blade tip.

Grid Type	Grid No.	Grid Points	% Grid Points
Rotor Blades	1-9	11,355,696	32.9
Center Body	10-12	1,915,518	5.5
L1 Wake	13-16	18,589,500	53.8
Brick	17-58	2,694,043	7.8
Total	1-58	34,554,757	100.0

Table 3 TRAM baseline structured overset grid system.

Figures 6-7 show a similar grid system that is used for the UH-60A four-bladed rotor. Figure 6a-b shows the rotor blade grids. Figure 6c shows a planform view of a rotor blade, including the inboard root, outboard trim tab, outboard swept tip, and locations of selected flight-test data. The Cartesian OB-grids shown in Fig. 7 are designed to capture the rotor wake in forward flight. Surface grid resolution is similar to the TRAM, with viscous wall spacing in the range of $0.5 \leq y^{+} \leq 1.0$.

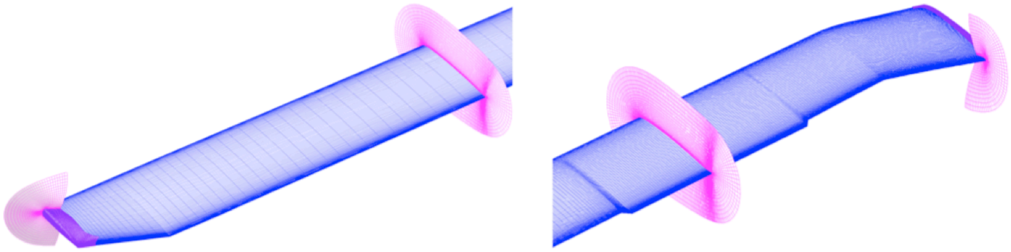

(a) Inboard view

(b) Outboard view

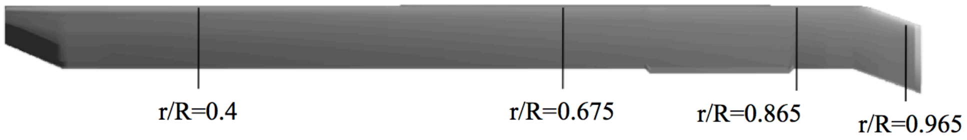

(c) Blade geometry with location of flight-test sectional loads.

Figure 6 UH-60A rotor grid system and location of flight-test data.

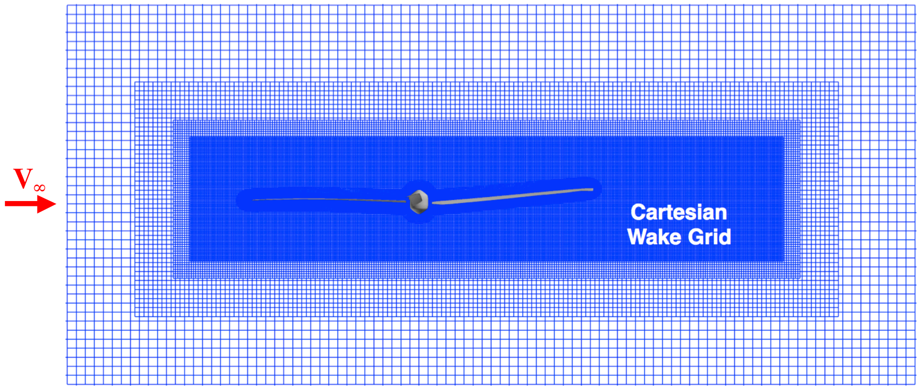

Figure 7. UH-60A Cartesian wake grids.

3.2 Numerical Accuracy

The Navier-Stokes equations can be written in strong conservation-law form as

$$\frac{\partial Q}{\partial t}+\frac{\partial(F-F_v)}{\partial x}+\frac{\partial(G-G_v)}{\partial y}+\frac{\partial(H-H_v)}{\partial z}=0 \tag{2}$$

where $Q=[\rho,\ \rho u,\ \rho v,\ \rho w,\ e]^T$ is the vector of conserved variables; F, G, and H are the inviscid flux vectors; and F_v, G_v, and H_v are the viscous flux vectors. An implicit approximate factorization scheme in delta form to solve Eq. (2) in generalized coordinates is given by

$$\left[I+h\partial_\xi \hat{A}^k\right]\left[I+h\partial_\eta \hat{B}^k\right]\left[I+h\partial_\zeta \hat{C}^k\right]\Delta\hat{Q}^k=-hR^{k,n} \tag{3}$$

where

$$R^{k,n}=\frac{3\hat{Q}^k-4\hat{Q}^n+\hat{Q}^{n-1}}{2\Delta t}+\left(\hat{F}-\hat{F}_v\right)_\xi^k+\left(\hat{G}-\hat{G}_v\right)_\eta^k+\left(\hat{H}-\hat{H}_v\right)_\zeta^k$$

and

$$h=\frac{2\Delta t\Delta\tau}{2\Delta t+3\Delta\tau}$$

In these equations, $\hat{Q}=Q/J$, where J is the transformation Jacobian, and $\hat{A}$, $\hat{B}$, and $\hat{C}$ are the transformed flux Jacobian matrices. The superscript *k* is the subiteration index, while the superscript *n* is the time-step index. The physical and pseudo (relaxation) time steps are Δt and $\Delta\tau$, respectively. Finally, $\Delta\hat{Q}^k=\hat{Q}^{k+1}-\hat{Q}^k$, where subiteration convergence implies that $\hat{Q}^k\rightarrow\hat{Q}^{n+1}$, which is 2nd-order accurate in time.

Equation 3 is solved using the Pulliam-Chaussee [11] diagonal algorithm. The V22 TRAM and UH-60A simulations use a time step of $\Delta t=¼°$ of rotation, with 20 and 40 subiterations respectively. This consistently achieved a 2.2-2.6 order subiteration drop between time steps for all NB grids. The OB Cartesian grids had substantially higher subiteration convergence. This is considered well converged in time (2-order drop is often sufficient) and ensures 2nd-order time accuracy. Throughout this subiteration process the Navier-Stokes algorithm becomes fully implicit and the approximate factorization and time linearization errors are sufficiently removed. Other investigators [12-13] have simulated the TRAM in hover with second-order time-accuracy using time steps of Δt=¼ and ½° of rotation.

Central differencing is used for all spatial operators throughout this paper. For example, the convective terms may use 6th-order central differences, and a 5th-order artificial dissipation term to damp out high-frequency errors. This results in a 5th-order accurate discretization on the uniform Cartesian OB grids. However, all viscous terms are evaluated with 2nd-order accurate central differences. The grid metrics on the curvilinear NB grids are also 2nd-order accurate in space. This discretization is referred to as 5th-order spatial differencing throughout this paper. Although the algorithm is still formally 2nd-order accurate in space, computed results show that this differencing scheme has lower diffusion and dispersion errors, and an improved flow field resolution than a 3rd-order approach. Table 4 summarizes the convective central difference operators available in OVERFLOW. Further details are described by Pulliam [14].

Cartesian Wake Grid Accuracy	Difference Stencil	Artificial Dissipation
$O(\Delta X^2)$	$\delta_X^{(2)}$	$\sim(\Delta X^3)\delta_{X^4}$
$O(\Delta X^3)$	$\delta_X^{(4)}$	$\sim(\Delta X^3)\delta_{X^4}$
$O(\Delta X^4)$	$\delta_X^{(4)}$	$\sim(\Delta X^5)\delta_{X^6}$
$O(\Delta X^5)$	$\delta_X^{(6)}$	$\sim(\Delta X^5)\delta_{X^6}$
$O(\Delta X^6)$	$\delta_X^{(6)}$	$\sim(\Delta X^7)\delta_{X^8}$

Table 4 Convective central difference operators.

3.3 Dynamic Adaptive Mesh Refinement

A new dynamic AMR capability has been included in OVERFLOW by Buning and Pulliam [15], where Cartesian grids are automatically added to the OB rotor wake grids to improve the resolution of the wake vortices. This is done internally to the OVERFLOW code in a time-accurate manner with moving rotor blades. This procedure is now briefly described using a feature-based scalar sensor function.

The concept of Level 1 grids and brick grids have already been introduced. The brick grids are successively coarsened by factors of two from the original Level 1 grid, to extend the computational domain to the far field. For example, if Δ_1 is a user-specified spacing for the Level 1 grids (baseline Cartesian wake grids), then the coarser brick grids have grid spacing of $\Delta_2=2\Delta_1$, $\Delta_3=4\Delta_1$, $\Delta_4=8\Delta_1$, and so on. In a similar manner, if a Level 1 region is identified for grid refinement, e.g., to better resolve a vortex core, then the grid spacing has the following form: $\Delta_{-1}=\frac{1}{2}\Delta_1$, $\Delta_{-2}=\frac{1}{4}\Delta_1$, $\Delta_{-3}=\frac{1}{8}\Delta_1$, and so on. This can be summarized by the following formula.

$$\Delta_L = \begin{cases} 2^{L-1}\Delta_1 & \text{where L} \ge 1 \\ 2^{L}\Delta_1 & \text{where L} \le -1 \end{cases} \qquad (4)$$

for any non-zero integer, L.

The dynamic AMR process can be summarized by the following set of rules:

Constraints

- Geometry cuts holes in L1 and finer grids
- Neighboring OB grids differ by only one level

At Each Grid Point

- Mark for refinement if a sensor value exceeds a refinement threshold (EREFINE)
- Mark for coarsening if a sensor value falls below a coarsening threshold (ECOARSEN)
- Mark only Level 2 and finer grids

Within an 8x8x8 Grid Cube

- If any point is tagged for refinement, refine the entire grid cube
- If all points are tagged for coarsening, coarsen the entire grid cube
- Grid cubes can only coarsen or refine by one level at a time

These rules determine if a grid cube should be refined, coarsened, or remain as it is. A user can specify a rectangular region to include or exclude AMR. This confines the use of AMR only to regions of interest.

Figure 8 is an example of an OVERFLOW dynamic AMR for the TRAM in hover. The vortices are rendered using the q-criterion and colored by vorticity magnitude. The grid resolution is shown on the y=0 cutting plane. This image corresponds to an instant of time in the early-stage evolution of the AMR process, which started from a baseline uniformly spaced L1-grid system.

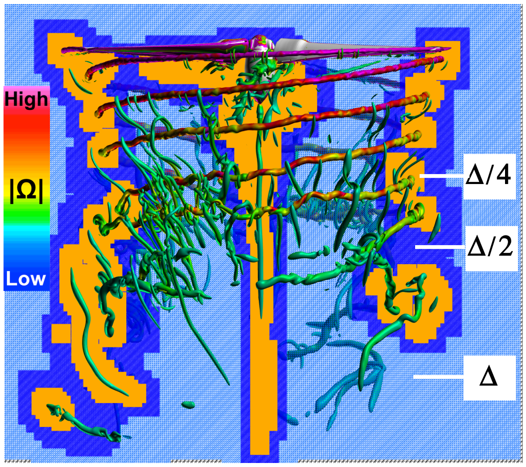

Figure 8 OVERFLOW two-level dynamic AMR grid system for the TRAM in hover. Vortices colored by vorticity magnitude, OB grid spacing Δ=10%ctip, Δ/2, Δ/4.

3.4 Turbulence Model

The rotor simulations presented in this study use the one-equation Spalart-Allmaras (SA) [4] turbulence model. Computed results will show that the details of the SA turbulence model play an important role in the numerical diffusion of the rotor tip vortices and the accurate prediction of FM. Some of the model's key features are described below.

The SA model uses the Boussinesq approximation to relate the Reynolds stresses to a kinematic turbulent eddy viscosity and the mean strain-rate tensor. The turbulent eddy viscosity (TEV) is given by

$$\nu_t = \tilde{\nu} f_{v1}$$

The SA transport equation for the variable $\tilde{\nu}$, is given by

$$\frac{D\tilde{\nu}}{Dt} = \underbrace{C_{b1}\tilde{\nu}\left(\Omega + \frac{\tilde{\nu}}{k^2 d^2} f_{v2}\right)}_{\text{Production}} - \underbrace{C_{w1} f_w \left(\frac{\tilde{\nu}}{d}\right)^2}_{\text{Dissipation}} + \underbrace{\frac{1}{\sigma}\left[\nabla \bullet \left(\left(\nu + \tilde{\nu}\right)\nabla\tilde{\nu}\right) + C_{b2}\left(\nabla\tilde{\nu}\right)^2\right]}_{\text{Diffusion}} \tag{5}$$

where *D*/*Dt* is the material time derivative. The right hand side consists of production, dissipation and diffusion source terms. The constants C_{b1}, C_{b2}, C_{w1}, k, σ, and functions f_{v1}, f_{v2}, f_w, are described by Spalart and Allmaras [4], and Ω is the magnitude of vorticity. The damping function, f_{v1}, reduces ν_t near a solid wall, i.e., the laminar sublayer. The turbulent length scale, *d*, is defined as the distance to the nearest wall.

Rotor blade vortices are a dominant structure in the turbulent rotor wake. They are initially formed at the rotor tip by the roll-up of the blade trailing edge shear layer. Figure 9 is a laser light sheet flow visualization of a fully formed tip vortex reported by Ramasamy et al. [16]. The rotor trailing edge wake shear layers (WSL) contain vorticity that is initially formed on the upper and lower surfaces of the rotor blades. The vorticity perpendicular to the vortex core is stretched and elongated as it is entrained into the vortex. This vortex stretching process can be thought of as a tube of vorticity whose diameter decreases as it elongates, resulting in higher levels of vorticity and turbulence, while conserving circulation. Ramasamy et al. [16] identified three regions of a developed vortex, which they show in Fig. 9. The outer region 3 can be characterized by a turbulent flow whose mean velocity field is similar to a potential vortex. Region 2 is an intermediate state that contains turbulent eddies of varying size. The inner-most region 1 can be characterized as stratified layers having few or small eddies with little interaction between fluid layers, due to high streamwise curvature. This inner-core region has a near-linear velocity profile and very low fluid strain. Gray [17-18] experimentally observed that the trailing edge WSL descends downward at a faster rate than the tip-vortex helix (see Fig. 10). This is due to an induced downwash by the thrust-producing rotor blades.

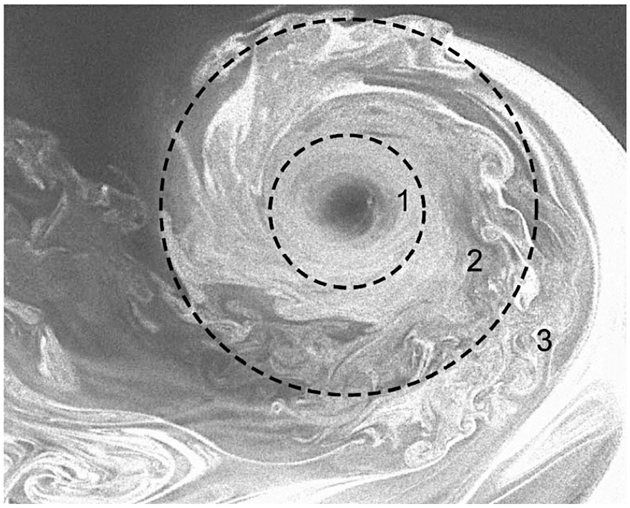

Figure 9 Laser light sheet flow visualization of a fully developed blade-tip vortex, Ramasamy et al. [16].

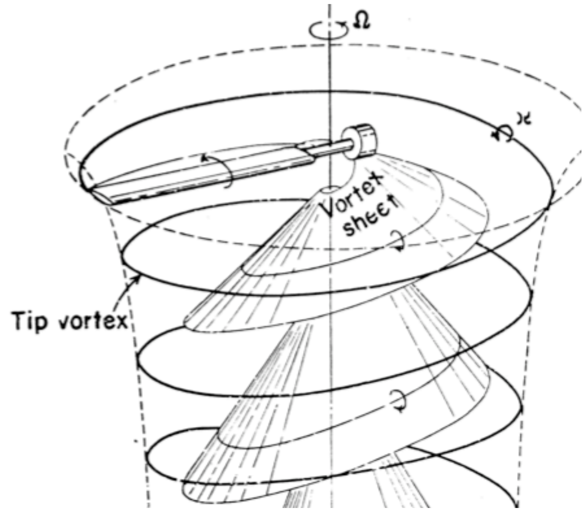

Figure 10 Sketch by Gray [17-18] of an observed descending wake shear layer.

Shur et al. [19] introduced a SA rotation and/or streamline curvature (SARC) correction for rotating and curved flows. The SARC correction not only improves the boundary layer profiles for highly curved flows, but also helps reduce the TEV in the tip vortex cores. This correction models the reduced mixing and very low strain in region 1 of Fig. 9. The SARC correction is used for all SA turbulent simulations in this paper.

An additional degree of realism can be obtained by the use of large eddy simulation (LES). In LES the largest turbulent eddies are resolved using a small grid spacing, Δ, and the subgrid-scale (SGS) eddies are modeled. Smagorinsky [20] first postulated a SGS model for the Reynold's stresses based on the following expressions

$$\tau_{ij} = 2\nu_t S_{ij},\ S_{ij} = \frac{1}{2}\left(\frac{\partial u_i}{\partial x_j} + \frac{\partial u}{\partial x_i}\right) \qquad (6)$$

where S_{ij} is the resolved strain-rate tensor, ν_t is the Smagorinsky eddy viscosity given by

$$\nu_t = \left(C_s\Delta\right)^2 \sqrt{S_{ij}S_{ij}} \qquad (7)$$

and C_s is the Smagorinsky coefficient. In this expression, $\Delta=(\Delta x\ \Delta y\ \Delta z)^{1/3}$, i.e., the geometric mean of the grid cell spacing. Use of LES throughout the entire computational domain is beyond the scope of flight Reynolds number rotor flows. This is due to the disparate length scales of wall-bounded flows, e.g., the boundary layer on a rotor blade. However, Spalart et al. [21] suggested detached eddy simulation (DES) as a more practical alternative.

DES can be viewed as a blending of a RANS turbulence model in boundary layers, together with coarse-mesh LES in regions of separated flow, or where the largest eddies are to be grid resolved. This is accomplished in the SA model by replacing the distance to the nearest surface (d) by

$$\bar{d} = \min\left(d, C_{DES}\Delta\right) \qquad (8)$$

where $\Delta=\max(\Delta x, \Delta y, \Delta z)$, and $C_{DES}=0.65$. In this way the SA-RANS model becomes the SGS model. Moreover, it is easy to see that when production balances dissipation in Eq. 5, and when $\bar{d}$ is used as the length scale, then ν_t simplifies to a Smagorinsky-type model. So the SA-DES model behaves like an LES-type model when the grid spacing is sufficiently small.

At this point a cautionary comment is in order. There is a potential danger in using DES in conjunction with excessive grid refinement near a solid wall, or a boundary layer gradually approaching separation. The intent of DES is to be in RANS mode throughout the boundary layer, where the turbulent scales can be very small and need to be modeled, and LES mode outside the boundary layer, where the largest turbulent scales are grid-resolved, e.g., separated flow. This occurs when the wall-parallel spacing is greater than the boundary layer thickness, $\Delta_{\|} > \delta$. If the wall-parallel grid spacing is much smaller than the boundary layer thickness ($\Delta_{\|} \approx \delta/20$ is a plausible starting point), then LES resolution applies within the upper portion of the boundary layer, and the RANS model is used closer to the wall. In-between these two examples, the grid spacing is ambiguous, being neither RANS nor LES. In these cases the turbulent shear stresses are too small within the boundary layer due to inadequate grid support for the full range of turbulent length scales. This modeled stress depletion (MSD) can trigger premature separation and give non-physical results.

This situation can be avoided by making sure the grid spacing parallel to the wall is larger than the attached boundary layer thickness. Spalart et al. [22] also introduced a correction called delayed detached eddy simulation (DDES). This algebraic formula prevents the inadvertent use of LES mode within a boundary layer, ensuring that the RANS model is active throughout that region. Details of the DDES modification are given in Ref. 22.

The DES approach has been used for some TRAM simulations, while DDES was used for the UH-60A simulation. In either case, the wall-parallel grid spacing is not so small as to require DDES. Nonetheless, DDES has been used in the UH-60A simulation as a precaution.

3.5 CFD/CSD Loose Coupling

The UH-60A rotor blade is highly flexible and responds to CFD loads and dynamic blade motions. Moreover, time-varying blade control angles must be iteratively determined to obtain prescribed thrust and hub moments for trimmed level flight. The CFD and CSD interaction is modeled by loosely coupling (LC) the OVERFLOW CFD code with the helicopter comprehensive code, CAMRAD II [23]. As the name implies, helicopter comprehensive codes provide a comprehensive engineering analysis for rotorcraft design, e.g., aerodynamics, structures, flight trim algorithm, flutter analysis, aeroacoustic analysis, etc.

CAMRAD II is widely used in the helicopter industry and models a flexible rotor blade using nonlinear finite elements. It has its own simplified aerodynamic model that uses lifting-line theory, a 2D airfoil table lookup for additional viscous realism, and vortex wake models. A complete rotor/hub solution for trimmed flight can be obtained in less than one minute using a single CPU.

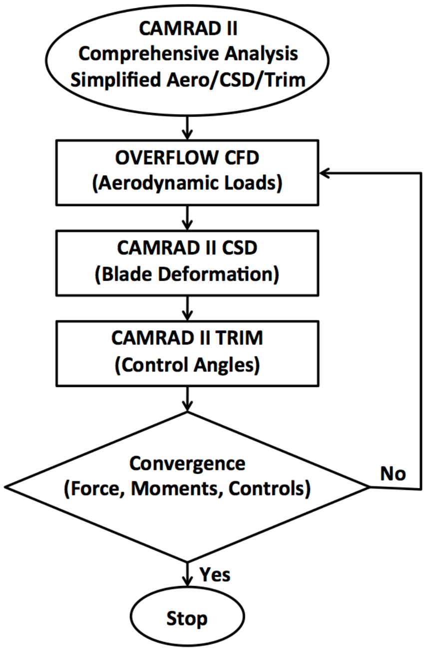

Figure 11 Loose coupling process for CFD/CSD/TRIM.

Improved, high fidelity, time-periodic solutions for the UH-60A rotor system are obtained by loosely coupling OVERFLOW with CAMRAD II (see Fig. 11). This coupling is done in a time-periodic manner, as specified by the user. The coupling period is some fraction of the number of rotor blades. In the case of the four-bladed UH-60A rotor, coupling periods of ¼, ½, and 1 revolution are typical. The lower coupling periods often provide faster LC convergence, provided the process is stable. More difficult cases, e.g., dynamic stall, may require larger coupling periods. A coupling period of ¼ revolution is used in this study.

A LC iteration involves OVERFLOW providing CAMRAD II with Navier-Stokes rotor blade loads. Then CAMRAD II provides OVERFLOW with a new set of blade deformations. If the forces, moments, and control angles are converged to the trim flight condition, then the LC is complete, otherwise another LC iteration is performed.

OVERFLOW airloads are transferred to CAMRAD II according to the expression

$$\begin{aligned}(F,M)^{l_c+1}_{Total} &= (F,M)^{l_c}_{CAero} + \left((F,M)^{l_c}_{CFD} - (F,M)^{l_c-1}_{CAero}\right)\\ &= (F,M)^{l_c}_{CFD} + \left((F,M)^{l_c}_{CAero} - (F,M)^{l_c-1}_{CAero}\right)\end{aligned} \tag{9}$$

where (F,M) corresponds to rotor blade sectional forces and moments at the 1/4-chord location. Superscript l_c is the LC step, subscript "*CAero*" refers to CAMRAD II aerodynamics model, and subscript "*Total*" refers to the total airloads applied to the deforming rotor blades within the CAMRAD II code. Note that as the LC process converges,

$$(F,M)_{Total} = \lim_{l_c\to\infty} (F,M)^{l_c}_{CFD} + \left((F,M)^{l_c}_{CAero} - (F,M)^{l_c-1}_{CAero}\right) = (F,M)_{CFD} \tag{10}$$

In other words, in the limit the total airloads applied to the flexible rotor blades within CAMRAD II are the OVERFLOW Navier-Stokes airloads. This process tends to converge rapidly, often within 3 rotor revolutions (using ¼-rev LC steps).

The CAMRAD II trim algorithm provides the blade root control angles for trimmed level flight. It accomplishes this by solving a nonlinear system of equations that describe the total force and moment response of the entire rotorcraft (in this case the rotor and hub) to perturbations in the control angles using the Newton-Raphson (NR) method. The NR gradient terms are obtained by numerically differentiating this equation with respect to the control angles. Prior to convergence, these gradients may differ somewhat from the OVERFLOW gradients, however, they are usually close enough for the process to converge. The purpose of the NR gradients is to move the updated control angles in the right direction to solve the nonlinear control-angle trim equations. Potsdam et al. [24] provide a detailed description of the delta airloads loose coupling process.

Finally, the assumption of time-periodic airloads on the rotor blades is a fundamental assumption to the time-accurate LC process. There may be some a-periodicity in the rotor wake, which is often the case, but the rotor blade airloads are required to be periodic. The LC process is therefore unable to simulate non-periodic vehicle maneuvers.

3.6 Vortex Visualization

A three-dimensional vortex is readily understood as a coherent swirling flow in the fluid dynamic literature. However, a precise time-dependent three-dimensional definition is surprisingly elusive. Jiang et al. [25] provide a good summary of several vortex visualization detection approaches. One approach often used in the rotorcraft community, and the one used here, is the q-criterion. Although its mathematical formula is well known, some investigators are less familiar with its origin and properties. A brief description is now given using Cartesian tensor notation.

The q-criterion is based on the velocity gradient tensor, which is given by

$$\frac{\partial u_i}{\partial x_j} = S_{ij} + \Omega_{ij} \tag{11}$$

where

$$S_{ij} = \frac{1}{2}\left(\frac{\partial u_i}{\partial x_j} + \frac{\partial u_j}{\partial x_i}\right), \text{ and } \Omega_{ij} = \frac{1}{2}\left(\frac{\partial u_i}{\partial x_j} - \frac{\partial u_j}{\partial x_i}\right)$$

are the strain-rate and spin tensors, respectively. The invariants of the velocity gradient tensor are obtained by solving the eigenvalue problem for Eq. 11, which leads to the characteristic equation

$$\lambda^3 - P\lambda^2 + Q\lambda - R = 0$$

where the roots, λ, are the eigenvalues, and the unique coefficients P, Q, and R, are the velocity gradient tensor invariants (with respect to coordinate rotation). The invariants are given by Kline et al. [26] as

$$P = u_{i,i} = \text{trace } (u_{i,j})$$

$$Q = \frac{1}{2}\left[P^2 - \text{trace } (u_{i,k}u_{k,j})\right]$$

$$R = \text{Det}\left(u_{i,j}\right)$$

The second invariant can be expressed as

$$Q = \tfrac{1}{2}[P^2 - \Omega_{ij}\Omega_{ji} - S_{ij}S_{ji}] = \tfrac{1}{2}[P^2 + \Omega_{ij}\Omega_{ij} - S_{ij}S_{ij}] = \tfrac{1}{2}[u_{i,i} + \left\|\Omega_{ij}\right\|^2 - \left\|S_{ij}\right\|^2] \tag{12}$$

where $\left\|S_{ij}\right\|^2$ and $\left\|\Omega_{ij}\right\|^2$ are the strain-rate and spin tensor magnitudes squared, respectively. The q-criterion is defined as the incompressible form of Eq. 12

$$q_c = \frac{1}{2}\left(\left\|\Omega_{ij}\right\|^2 - \left\|S_{ij}\right\|^2\right) \tag{13}$$

Using Eq. 13 in compressible flows may cause some confusion. It is used mostly for historical reasons as earlier applications were for incompressible flows. Neglecting the dilatation term has no significant affect on visualizing the shape of a vortex, since compressibility affects are much smaller than the spin and strain-rate tensors. The q-criterion, Eq. 13, is also invariant with coordinate rotation for compressible flows because it is constructed from the magnitudes of two tensors. Moreover, the q-criterion is Galilean invariant because it only contains velocity gradient terms. Galilean and rotational invariance is a favorable property that insures the viewed vortex does not depend on reference frame translation or orientation. Positive iso-surfaces of the q-criterion emphasize vortices while negative values emphasize fluid strain rate. The q-criterion can be expressed in Cartesian coordinates by the expression

$$q_c = -\frac{1}{2}\left[\left(\frac{\partial u}{\partial x}\right)^2 + \left(\frac{\partial v}{\partial y}\right)^2 + \left(\frac{\partial w}{\partial z}\right)^2\right] - \left(\frac{\partial u}{\partial y}\right)\left(\frac{\partial v}{\partial x}\right) - \left(\frac{\partial u}{\partial z}\right)\left(\frac{\partial w}{\partial x}\right) - \left(\frac{\partial v}{\partial z}\right)\left(\frac{\partial w}{\partial y}\right) \tag{14}$$

This formula requires less memory and fewer function evaluations than Eq. 13, when programed into commercial flow visualization software.

4. Results and Discussion

The OVERFLOW CFD code is used throughout this study to solve the time-dependent Navier-Stokes equations for isolated rotors in hover and forward flight. Unless noted otherwise, the viscous Navier-Stokes equations are applied throughout the entire computational domain using 2nd-order time accuracy and 5th-order central differences for the inviscid convective terms, as described in the Numerical Accuracy section. Vortices are visualized using iso-surfaces of the q-criterion. Attention will first be directed to the rigid V22 TRAM rotor and then the flexible UH-60A helicopter rotor.

4.1 V22 TRAM Rotor in Hover: θ=14°

OVERFLOW simulations for the V22 TRAM rotor in hover are used to assess the effects of 3rd and 5th-order spatial differences, and blade surface resolution. The collective pitch angle is θ=14°, the blade tip Mach number M_{tip}=0.625, and the Reynolds number based on tip chord Re=2.1 million. This corresponds to a high-thrust wind-tunnel condition [7-8], where the measured figure of merit is FM_{EXP}=0.780.

The OVERFLOW simulations reported by Holst and Pulliam [1] (see Fig. 2) used 3rd-order spatial differences with the SA-RANS turbulence model. Moreover, they treated the OB Cartesian grids as inviscid to reduce vortex diffusion in the wake. For the moment, the same approach is taken here to allow for a direct comparison with their results. The surface-grid resolution for this computation is similar to the finer surface grids in Fig. 2b and the coarser wake-grid spacing in Fig. 2a, i.e., Δ=10%c_{tip}. This results in a computed figure of merit of FM=0.777, similar to the FM in Fig. 2b. So the improvement in predicted FM in Fig. 2b over that of Fig. 2a is due to the higher NB grid resolution on the rotor blades, not the higher wake-grid resolution. In other words, it is more important to get the vortex strength right at the blade tip. Highly resolving the vortex wake will reduce vortex diffusion but not improve the prediction of FM. Table 5 summarizes all TRAM OVERFLOW results reported in this study for the 14° collective. All further OVERFLOW results reported in this study solve the time-dependent Navier-Stokes equations throughout the entire computational domain, including the Cartesian wake grids.

Figure 12 shows the effects on the FM and rotor wake using three different spatial difference strategies. Note that the FM for the 5th-order solution is more accurate than the 3rd-order solution, and resolves the rotor wake in much greater detail. When 3rd-order/5th-order spatial differences are used on the NB/OB grids,

Description	Fig	NB Grid	OB Grid	FM
DNW Test [7-8]	3	NA	NA	0.780
½ resolution NB grids [1]	2a	3rd-O RANS	3rd-O Euler	0.73
AMR3 [1] Δ_{-3}=1.25%c_{tip}	2b	3rd-O RANS	3rd-O Euler	0.77
Baseline Grid	NA	3rd-O RANS	3rd-O Euler	0.777
Baseline Grid	12a	3rd-O RANS	3rd-O RANS	0.733
Baseline Grid	12b	5th-O RANS	5th-O RANS	0.777
Baseline Grid	12c	3rd-O RANS	5th-O RANS	0.730
Baseline Grid	22a	5th-O DES	5th-O DES	0.778
AMR2 Δ_{-2}=2.5%c_{tip}	22c	5th-O DES	5th-O DES	0.780

Table 5 Summary of DNW data (M_{tip} =0.62) and OVERFLOW (M_{tip} =0.625) FM. θ=14°, Re=2.1 million.

the FM accuracy and wake resolution drop back to the pure 3rd-order result (see Fig. 12a, c). Once again it is seen that improved spatial accuracy on the body grids is more important than resolving the rotor wake for predicting FM. The figure of merits shown in Figs. 2b and 12b are of similar accuracy. However, Fig. 2b uses 448 million grid points with 3rd-order differences, while Fig. 12b only uses 35 million grid points with 5th-order differences. The computational expense of AMR wake grids is not needed to accurately predict FM.

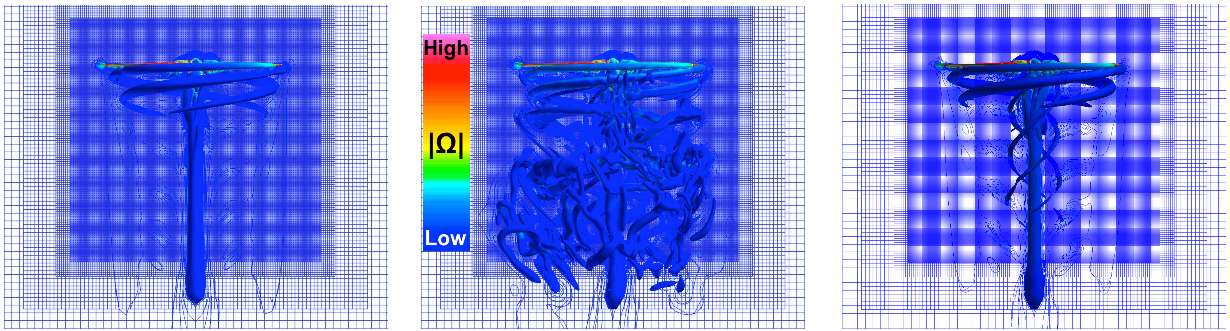

a) 3rd-order, FM=0.733. b)5th-order, FM=0.777. c)3rd/5th-order NB/OB, FM=0.730.

Figure 12 Effect of different differencing strategies on the FM, rotor vortices, and vorticity contours at the y=0 cutting plane. TRAM OVERFLOW simulations in hover, $M_{tip}=0.625$, $\theta=14^\circ$, Re=2.1 million.

4.2 V22 TRAM Rotor in Hover: $6^\circ \leq \theta \leq 16^\circ$

The previous section focused on the 14 degree high-thrust collective, and showed the importance of resolving the formation of the tip vortices with fine body grids and high-order spatial differencing. It was also shown that the FM could be accurately computed for this flow condition, even when applying the RANS equations throughout the entire computational domain, see Table 5 and Fig. 12b. Now the focus is on computing FM for a range of collectives, and comparing the results with experiment and the FUN3D and HELIOS CFD codes. A brief description of each code's solution strategy is now given.

OVERFLOW solves the time-accurate Navier-Stokes equations for the TRAM rotor in hover using 2nd-order time accuracy, 5th-order central differences, and the SA turbulence model. Further details are provided in the Numerical Approach section.

FUN3D [27-29] solves the time-dependent Navier-Stokes equations with 2nd-order spatial accuracy on unstructured overset grids. Lee-Rausch and Biedron [12] simulated the flow for the TRAM rotor in hover using the steady SA-RANS equations throughout the entire computational domain. The steady equations use a non-inertial coordinate system for improved computational efficiency. They use the Dacles-Mariani [30] correction to reduce the TEV in the vortex core.

HELIOS [31] can be characterized as a highly modular framework designed for rotorcraft applications. It uses an unstructured 2nd-order accurate solver for the body grids, and a 5th-order accurate structured Cartesian-grid solver in the rotor wake region, similar to OVERFLOW. This approach combines the benefits of treating complex geometries in a more automated manner with an unstructured-grid module, and improved spatial accuracy and solution efficiency in the rotor wake region with a structured Cartesian-grid module. Wissink et al. [13] simulated steady flow for the TRAM rotor in hover using the SA-RANS equations on the rotor unstructured body grids, and the inviscid Euler equations on the structured Cartesian vortex-wake grids. The inviscid approximation in the wake is used to reduce vortex diffusion. Like FUN3D, the Helios TRAM simulations were run in steady mode using a non-inertial frame of reference for improved computational efficiency.

Figure 13 shows the FM variation with thrust coefficient (C_T) for OVERFLOW, FUN3D, HELIOS and the DNW wind-tunnel test [7-8]. The experimental error in FM is estimated to be about ±0.005, Ref. [32]. CFD solutions were carried out at collectives varying from 6°-16°, at two-degree intervals. (The approximate locations of the collective angles are indicated at the top of the figure.)

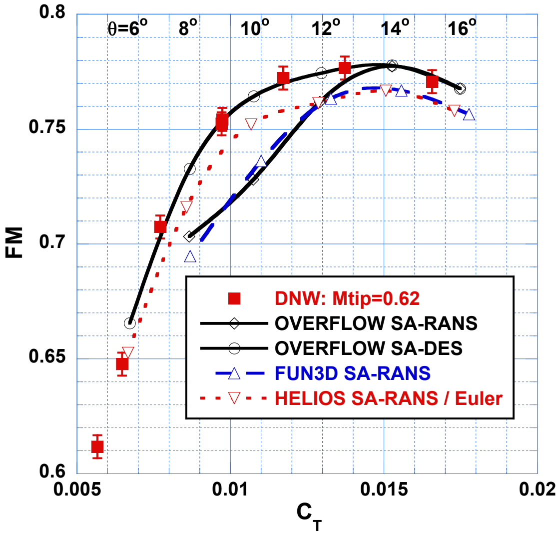

Figure 13 Figure of merit variation with C_T for the TRAM rotor in hover. M_{tip}=0.625, Re=2.1 million.

The OVERFLOW FM computed using the SA-RANS turbulence model are in excellent agreement with the DNW data at the 14° and 16° collectives. However, the FM values significantly under-predict the measured values at the lower collectives (θ=8°-12°). The FUN3D and HELIOS codes under-predict FM for all collectives using the SA-RANS turbulence model. The use of 2^{nd}-order spatial accuracy is probably responsible for the under-prediction of FM at the higher collectives. HELIOS is in better agreement with the data at the lower collectives, but this is attributed to the ad-hoc inviscid approximation in the wake grids. None of the SA results accurately predicts the FM for all collectives.

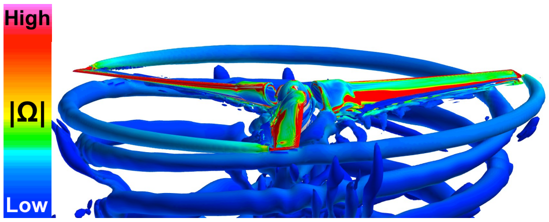

Figure 14 OVERFLOW Vortices rendered with the q-criterion. M_{tip} =0.625, Re=2.1 million, θ=10°, SA-RANS turbulence model.

The largest discrepancy between the OVERFLOW SA-RANS FM and the DNW data occurs at θ=10°. Two observations can be made. First, there is significant blade vortex interaction (BVI) for collectives below 14°. This can readily be seen in Fig. 14, for θ=10°, where the rotor blade strikes the tip vortex from the previous blade. Second, the TEV is more elevated for the BVI collectives than the non-BVI collectives [5]. This suggests a problem with the SA-RANS turbulence model.

The problem can be traced to the SA-RANS turbulent length scale, *d*, which is the distance to the nearest solid surface. This length scale, which was originally developed for boundary layer flows, is supposed to represent an estimate of the largest energy-bearing eddies (see Fig. 15a). However, in the rotor wake the length scale can be very large, even several rotor radii (see Fig. 15b). Under these conditions, Eq. 5 can have large amounts of turbulent production without turbulent dissipation, leading to excessive TEV in the wake. The length scale has simply become a geometric parameter.

The DES length scale in Eq. 8 is an attractive alternative to the RANS length scale in the turbulent rotor wake. As the wake grids are refined, more turbulent eddies are resolved, and the remaining sub-grid scales are modeled by the SA turbulence model using Eq. 8. Even if the wake grids are too coarse to model the largest turbulent eddies, the DES length scale is considerably more realistic than the distance to the nearest wall. The levels of TEV are greatly reduced in a rational, physics-based manner.

The OVERFLOW FM using SA-DES is also shown in Fig. 13. The agreement with the measured FM is excellent for all collectives. This marked improvement in the prediction of FM, compared to the SA-RANS model, is now within experimental error for the first time [5] for a wide range of collective angles. These baseline Cartesian wake grids have a grid spacing of Δ=10%c_{tip}, about the size of the physical vortex core diameter formed at the rotor blade tip. This coarse wake-grid spacing is not resolving the turbulent eddies that are entrained into the tip vortex, see for example Fig. 9. Rather, the DES length scale is simply more realistic than the RANS length scale, allowing the turbulent production and dissipation terms to be in balance, and therefore reducing the TEV in the wake to more physically appropriate levels.

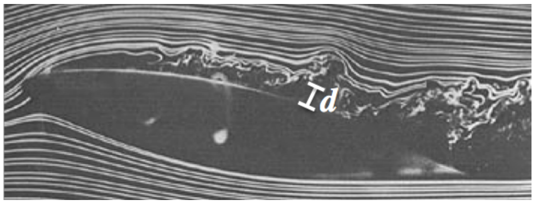

a) Turbulent boundary layer on an airfoil.

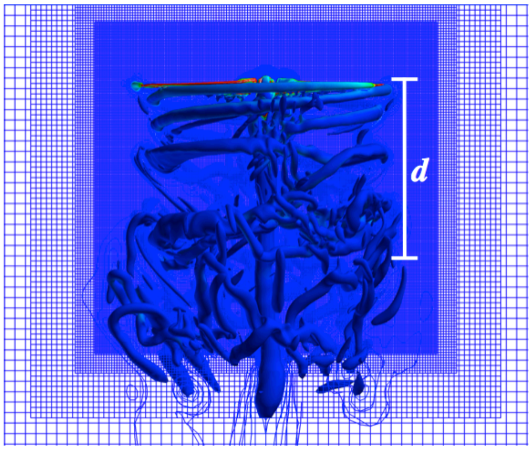

b) Turbulent rotor wake.

Figure 15 Different SA-RANS turbulent length scales.

Figure 16 shows the BVI process that generates large TEV levels in the rotor wake, which in turn reduce the rotor FM. The solution begins in Fig. 16a with the SA-DES result, and then OVERFLOW is switched to the SA-RANS model. The vortices and y=0 cutting plane are colored by Log(TEV). Each integer increment represents an order-of-magnitude increase in TEV. Notice that the rotor wake initially has a relatively low TEV, ~100. This is due to the reduced DES turbulent length scale, Eq. 8. The TEV grows with time, especially in the lower wake (see Fig. 16b). This is due to the larger RANS turbulent length scale turning off the turbulent dissipation in Eq. 5. Eventually the elevated TEV works its way up to the top of the vortex wake (see Fig. 16c). The elevated TEV are not instantaneous, but take time to build up through the convective process governed by Eq. 5. Figure 16 represents 10 rotor revolutions in time. BVI allows the large TEV to enter the rotor blade boundary layer. When this happens, C_T remains about the same but C_Q increases due to an increase in drag. This causes the FM to decrease, see Eq. 1. When there is no BVI, the vortices and any high TEV pass cleanly under the blades and the FM remains unchanged.

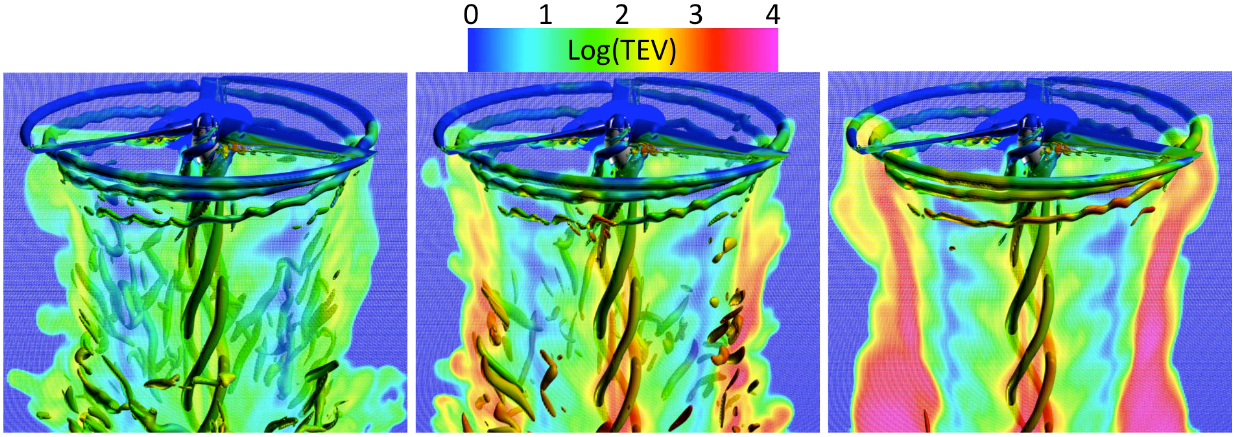

a) SA-DES. b) Transitional. c) SA-RANS.

Figure 16 Progression of TEV growth from SA-DES to SA-RANS. M_{tip}=0.625, θ=10°, Re=2.1 million.

4.3 V22 TRAM Rotor in Hover: AMR

The SA-DES turbulence model with the SARC correction has been shown to provide appropriate physics-based levels of TEV throughout the entire computational domain. Throughout the remainder of this study, the time-dependent Navier-Stokes equations are solved in OVERFLOW using 2nd-order time accuracy, 5th-order spatial differences, and the SA-DES turbulence model with the SARC correction. The viscous terms are applied throughout the entire computational domain.

Dynamic AMR is now used to resolve the rotor wake for the TRAM in hover using a vorticity magnitude sensor function. The flow conditions are: M_{tip}=0.625, θ=10° and 14°, Re=2.1 million. A baseline grid solution uses a constant OB Cartesian grid spacing of Δ=10%c_{tip}, i.e., no AMR. One level of refinement (AMR1) uses OB Cartesian grid spacings of Δ=10%, and 5%c_{tip}. Two levels of refinement (AMR2) uses OB Cartesian grid spacings of Δ=10%, 5%, and 2.5%c_{tip}. The grid sizes are summarized in Table 6. An AMR result is started from a baseline result and run until the FM converges, which typically requires another 10 revolutions. The time step is Δt=¼° with 20 subiterations, which gives at least a 2.2-order subiteration drop between time steps.

The computed FM is quantified in Table 7 using a running mean and standard deviation based on one rotor revolution. Figure 17 shows a typical baseline FM and standard deviation convergence with time (revs). One standard deviation is about 0.002, which means the third digit is significant. Note that there is little variation between the baseline and AMR FM for both collectives. This is consistent with the earlier conclusion that wake-grid resolution has little affect on FM. The AMR2 FM for θ=14° is now in precise agreement with FM_{EXP}=0.780. However, it is worth noting that the experimental error is about 0.005 [32]. Figure 17 and experience with other solutions indicate that FM can be computed to two significant digits in about 10 revolutions from an impulsive start condition. However, three-digit accuracy typically requires 20-30 revolutions.

OB Grids	Number of Grids	Number of Grid Points
Baseline	58	35 million
AMR1	~2,400	105 million
AMR2	~14,000	670 million
Δ_l=2.5%c_{tip}	589	1.3 billion

Table 6 Grid sizes, M_{tip}=0.625, θ=14°, Re=2.1 million.

Collective	OB Grids	FM running mean	Standard Deviation (σ)	Difference from Baseline
10°	Baseline	0.764	0.002	0
10°	AMR2	0.763	0.002	-0.001
14°	Baseline	0.778	0.002	0
14°	AMR1	0.778	0.002	0
14°	AMR2	0.780	0.002	+0.002

Table 7 Summary of selected OVERFLOW SA-DES FM. M_{tip}=0.625, Re=2.1 million.

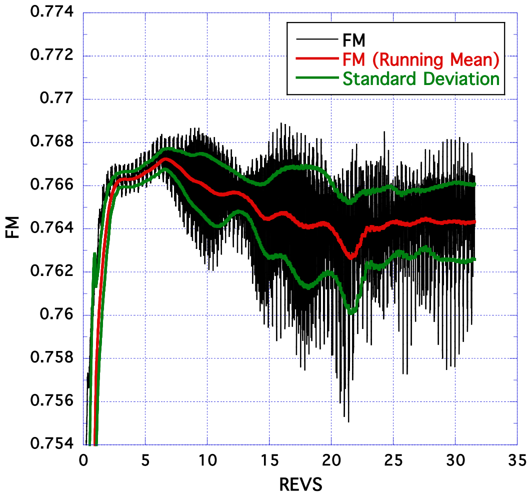

Figure 17 Convergence of OVERFLOW SA-DES FM. M_{tip}=0.625, θ=10°, Re=2.1 million.

Figure 18 is a flow visualization of the 14° collective AMR2 wake. This two-level refinement shows vortices that are stronger and smaller in diameter than the baseline result in Fig. 12b. There are also several inboard vortices that correspond to the blade root tip and local geometry changes. Figure 19 is a cut-away view of the vortex wake. The horizontal interior bands are cuts through the TE WSL spiraling downward from each rotor blade. Small turbulent "worms" are also prevalent along the cylindrical vortex wake slip line, which were first reported by Chaderjian and Buning [5]. The turbulent wake spreading rate in Fig. 19 resembles a turbulent jet.

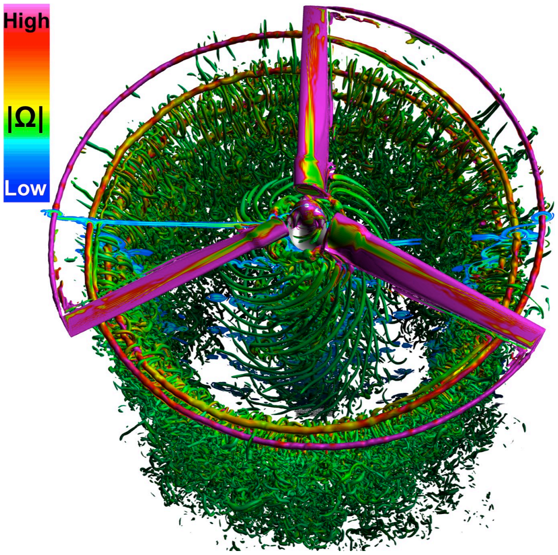

Figure 18 Downward view of vortex wake. $M_{tip}=0.625$, $\theta=14°$, Re=2.1 million, FM=0.780.

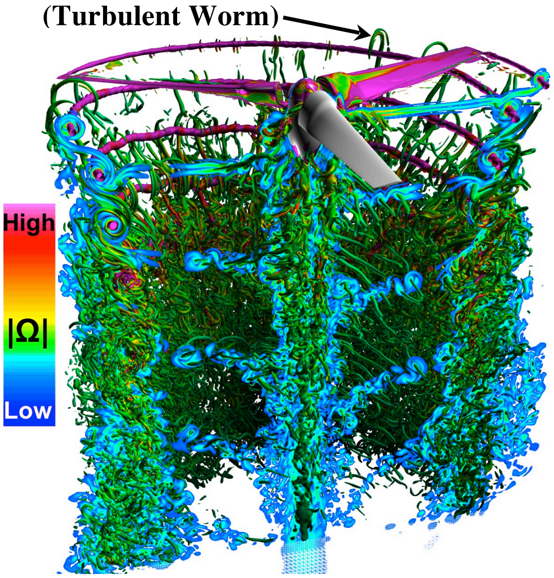

Figure 19. Cut-away view of vortex wake. $M_{tip}=0.625$, $\theta=14°$, Re=2.1 million, FM=0.780.

A rotor blade WSL is found to move downward at a greater rate than the tip vortex helix. This well known effect was first observed experimentally by Gray [17] in 1956 and is due to the strong downwash from the thrust-generating rotor. Figure 20 is a photograph from Gray's lecture [18]. He conducted an experiment with a single rotating blade, where the vortex wake was made visible by smoke emitted from the rotor tip. The WSL is clearly visible in the photograph. Small vortical worms appear to be circling the vortex cores, similar to those shown in Figs. 18-19. This "interpretation" of the smoke visualization provides plausible physical evidence for the computed worm structures.

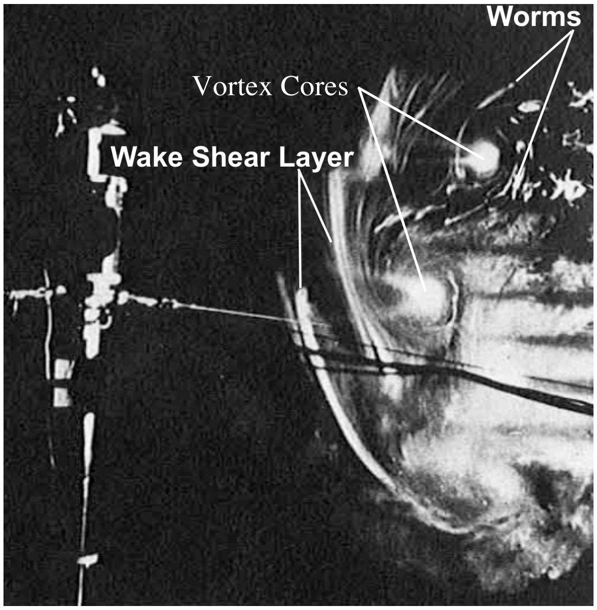

Figure 20 Photo of Gray's single-blade rotor experiment [17-18]. Smoke is used to visualize the vortex wake.

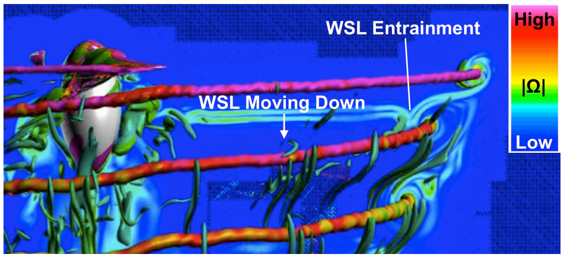

a) Wake shear-layer entrainment.

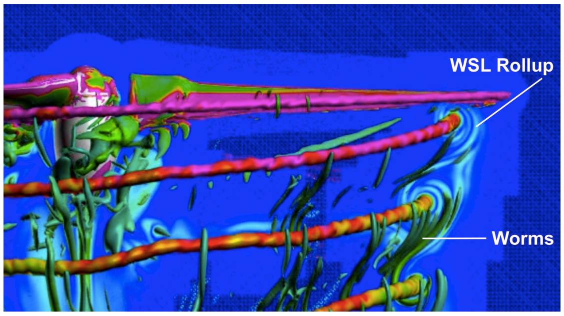

b) Worms and wake shear-layer rollup.

Figure 21. Two frames from a CFD animation. $M_{tip}=0.625$, $\theta=14°$, Re=2.1 million.

The fluid mechanism for the formation of vortical worms can be determined from a CFD animation of the flow. Two frames from the animation are shown in Fig. 21. As the WSL descends and passes by a vortex core, it is first pinched and then a portion is detached from the WSL. This detached shear layer then rolls up and is entrained into the vortex core. This process has two effects. First, the WSL is constantly being pulled radially outward toward the tip vortices. Second, the vorticity in the WSL that is perpendicular to the vortex core is stretched. Vortex stretching causes the vorticity magnitude to increase through conservation of angular momentum. This renders the vortical worm visible though an iso-surface of the q-criterion (Fig. 21) or smoke visualization (Fig. 20). Notice that in Fig. 21b, the worms line up precisely with the shear-layer rollup. These rolled-up shear-layers are simply the two-dimensional cross-sectional view cutting longitudinally through the cylindrical worms.

Figure 22 shows the progression of vortex wake complexity with wake-grid refinement. The dynamic AMR process is capturing the pertinent vortical structures in Figs. 22b-c. The finer AMR2 grids are also resolving the TE WSL. The uniform baseline wake grid is too coarse to resolve any turbulent worms. Worms first appear with the AMR1 grid and become more numerous with the AMR2 grid. The largest AMR2 worms are 15% smaller in diameter than the AMR1 worms. Both the AMR1 and AMR2 worms have 7% of the tip vortex vorticity magnitude. The reference vorticity was taken at a 10° wake age from the rotor blade tip. The worm diameter and vorticity magnitude were difficult to characterize and should be considered approximate.

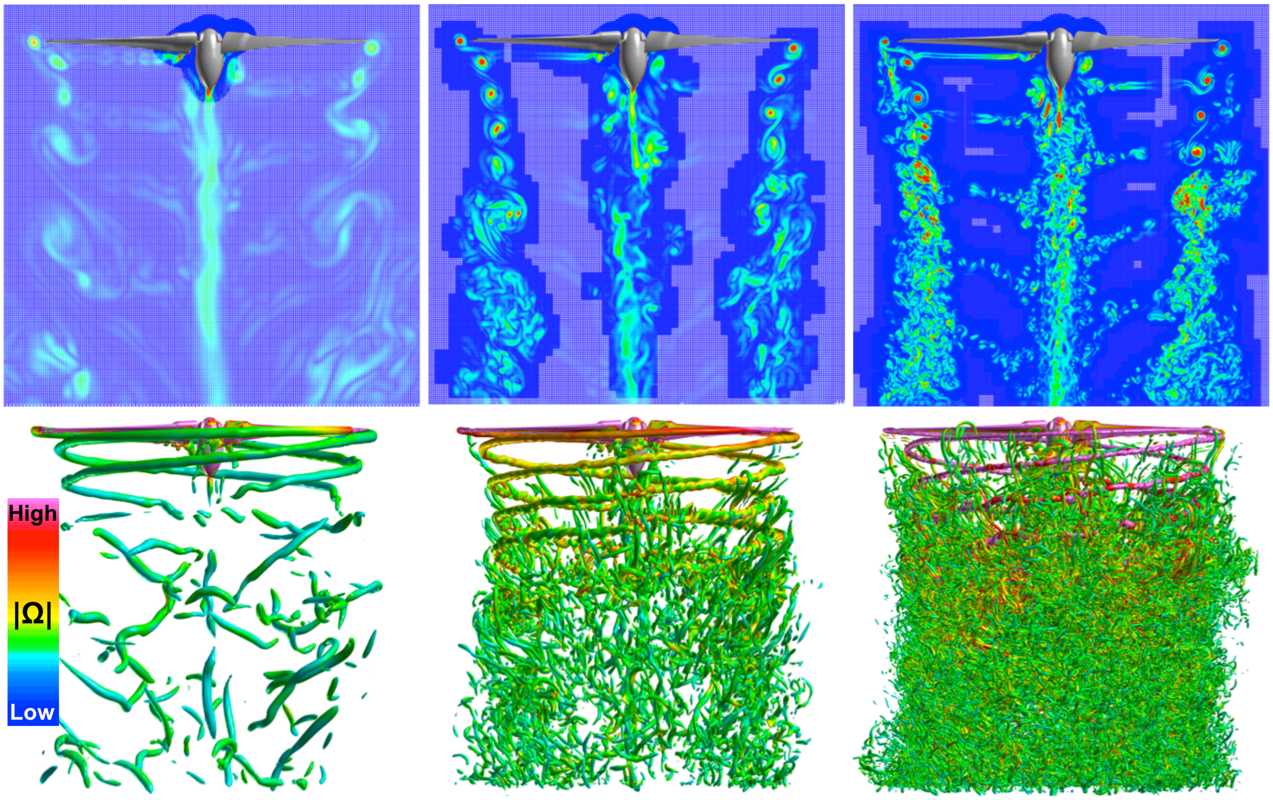

a) Baseline, FM=0.778. b) AMR1, FM=0.778. c) AMR2, FM=0.780.

Figure 22 Baseline, AMR1, and AMR2 OVERFLOW solutions for the TRAM in hover: M_{tip}=0.625, θ=14°, and Re=2.1 million. Vorticity contours on the y=0 cutting plane, and vortices in the wake.

The AMR2 worms are more numerous and smaller in diameter than those found in the AMR1 simulation. This is expected, as the finer DES meshes resolve smaller turbulent scales. The notion of DES grid independence is different from that of a RANS simulation. Since all the turbulent scales are modeled with the RANS approach, grid refinement will eventually result in no further changes in the wake. On the other hand, rotor loads and the largest worms should be resolved as one refines the DES mesh.

Figure 23 compares the AMR2 result (Δ=10%, 5%, and 2.5%c_{tip}) with a uniform L_1 grid spacing (Δ_1=2.5%c_{tip}). The vorticity contours are virtually identical on the upper portion of the wake, and very similar in the lower wake. Most of the small differences in the lower wake are probably due to the chaotic nature of turbulence. This demonstrates that the use of linear interpolation from a coarse AMR mesh to a fine AMR mesh does not alter the flow in any significant way. This interpolation is only used far away from the vortical structures, where flow gradients are small. In the vicinity of the vortex structures, the grid is uniform and no interpolation is required.

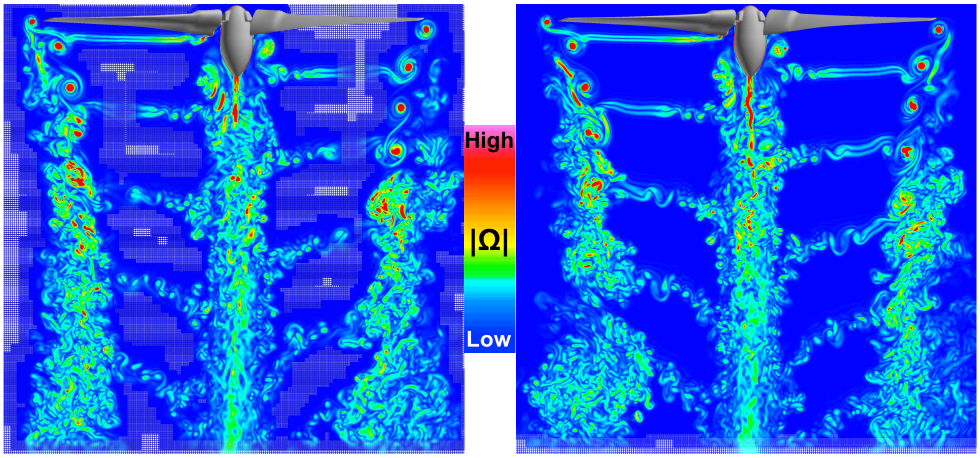

a) AMR2, Δ=10%, 5%, and 2.5%c_{tip}. b) Uniform wake grid, Δ_1=2.5%c_{tip}.

Figure 23 Comparison of AMR2 and uniform wake grid for TRAM in hover: M_{tip}=0.625, θ=14°, and Re=2.1 million. Vorticity contours on the y=0 cutting plane.

Figure 24 shows the formation of the AMR2 rotor blade vortex for θ=14°. The vortex first forms near the blade trailing edge, and resembles a rope braid consisting of vorticity from the upper and lower-surface boundary layers. The "braided" vortex then transitions into a circular form. The NB curvilinear grids overlap with the OB Cartesian grids behind the blade TE and appear as a small iso-surface patch. The smooth transition of vortex core size indicates the two overset grid resolutions are well matched.

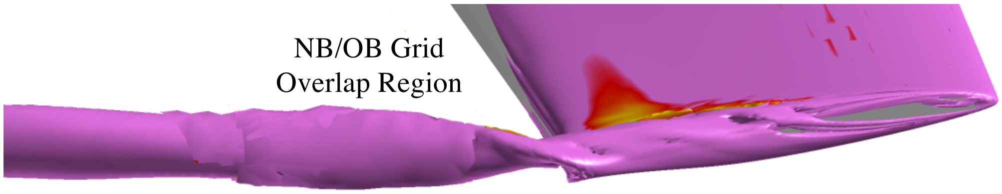

Figure 24 Tip vortex formation for the AMR2 wake grid. TRAM rotor in hover: M_{tip}=0.625, θ=14°, and Re=2.1 million.

Figure 25 shows velocity vectors on cross-flow cutting planes, which are colored by vorticity magnitude. These cutting planes are at two wake ages, ψ_w=30° and 390°, defined as the azimuthal angle from the rotor blade trailing edge. The green patterns are the WSL entrainment (roll-up) into the tip vortices. Even at an early wake age, Fig. 25a, the vortex core shape is exhibiting some distortion. The vortex core shape has greater distortion at a later wake age (see Fig. 25b). This distortion from the ideal circular pattern is due to complex vortical and turbulent worm interactions in the wake. In fact, the vortex core is undergoing vortex pairing with another tip vortex that is above it and out of view of the figure. Figure 26 shows the cross-flow velocity across each of the vortices in Fig. 25. The velocity asymmetries are evident. The symbols represent values take from the OB Cartesian grid and therefore indicate the Cartesian grid spacing. The near wake-age and far wake-age vortices each have 8 and 14 grid cells of resolution, respectively.

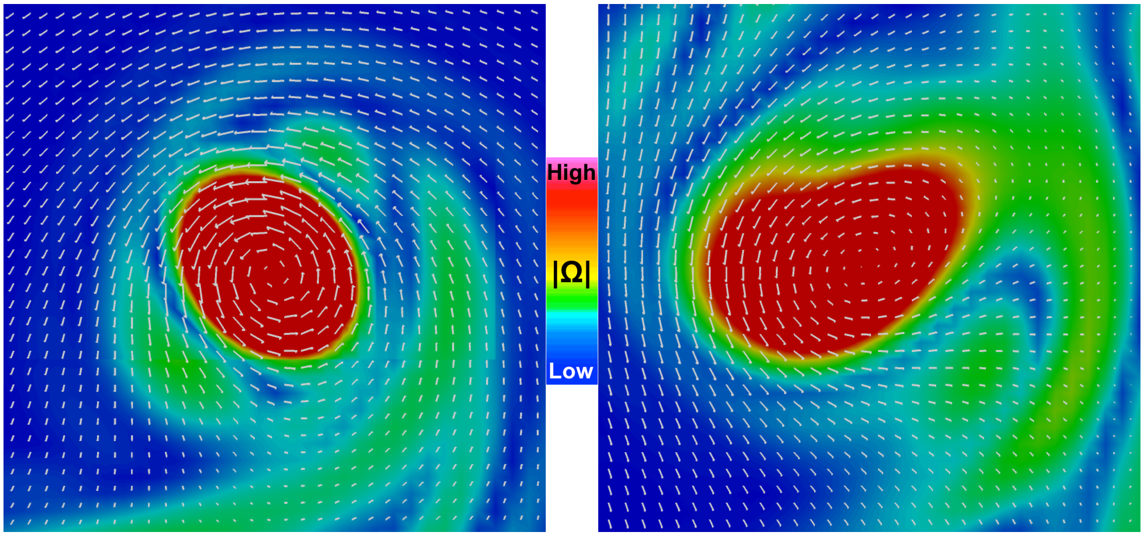

a) 30° wake age.

b) 390° wake age.

Figure 25 Velocity vectors and vorticity contours. M_{tip}=0.625, θ=14°, and Re=2.1 million.

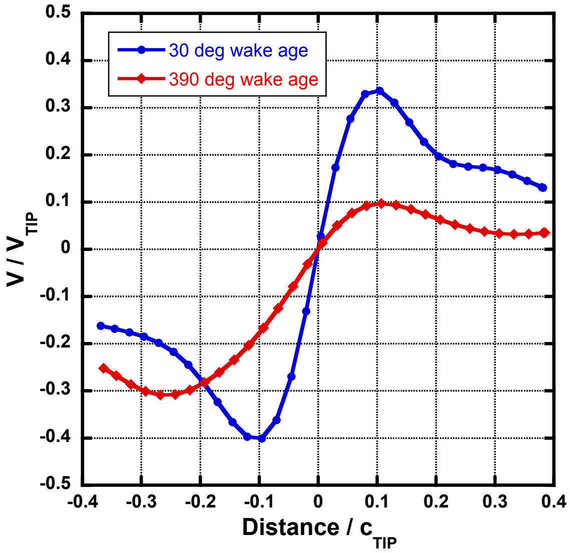

Figure 26 Cross-flow velocity. M_{tip}=0.625, θ=14°, Re=2.1 million.

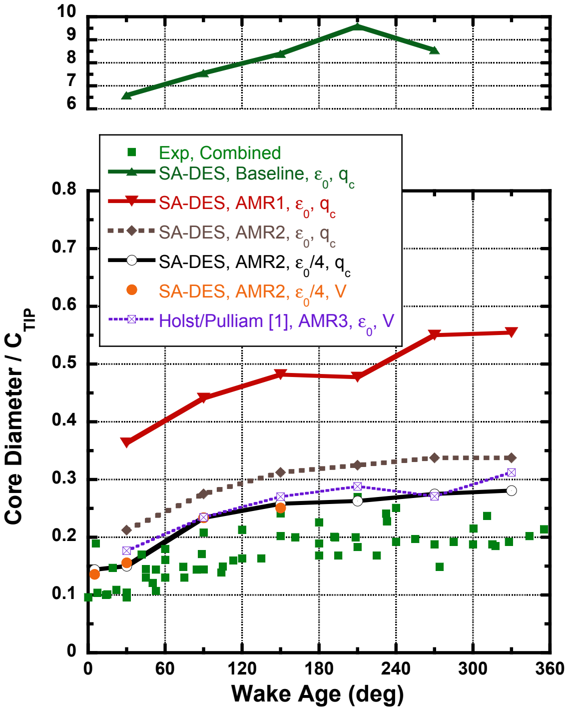

Figure 27 Vortex core growth with wake age. M_{tip}=0.625, θ=14°, Re=2.1 million.

Figure 27 shows the normalized vortex-core diameter variation with wake age for different OB wake-grid resolutions. The experimental data is obtained from Refs. [33-35]. The baseline central-difference artificial dissipation level is designated as ε_o (DIS2=0.0, DIS4=0.2, Ref. [3]). The vortex core size is defined as the distance between cross-flow velocity peaks, e.g., Fig. 26, and is designated as "V" in Fig. 27. Another approach is to use the q-criterion. The q-criterion value can be selected to give the same vortex core size as the velocity-peak approach, see $\varepsilon_o/4$ results in Fig. 27, and is designated as q_c in the figure. The q-criterion approach is preferred in this study because velocity peaks may be difficult to find at greater wake ages. The horizontal and vertical directions can be used to obtain an average core size. The q-criterion iso-surface level, when large enough, is not very sensitive to core size.

The baseline wake resolution (Δ=10%c_{tip}) has core sizes that are more than an order-of-magnitude larger than the measured data. This is not surprising since this resolution only has one grid cell across the physical vortex core at an early wake age. The numerical vortex core is diffused. The AMR1 result (Δ=10%, and 5%c_{tip}) shows a dramatic improvement in the predicted core size. The AMR2 result (Δ=10%, 5%, and 2.5%c_{tip}) is closer still. Reducing the artificial dissipation to the lowest possible level (to maintain code stability) has the computed core sizes skimming along the top of the experimental data. This is similar to the Holst/Pulliam [1] AMR3 result (Δ=10%, 5%, 2.5, and 1.25%c_{tip}).

Table 8 summarizes a regression exponential curve fit for the vortex core diameter data in Fig. 27, where $D \propto \psi_w^P,\ \psi_w \ge 30^\circ$. The exponent, P, represents the vortex core growth rate, and compares more favorably with experiment as the wake-grid is refined. The AMR2-$\varepsilon_o/4$ growth-rate is in very close agreement with the experimental value. The Holst/Pulliam [1] result is in between the two AMR2 results. This discrepancy is probably due to their use of 3rd-order spatial accuracy, and possibly the close proximity of the lower L_1 wake-grid boundary, which is located about 0.6 R below the rotor disk.

Case	Finest Grid Spacing	Regression Exponent
Exp	NA	0.25
Baseline, ε_o	10%c_{tip}	0.15
AMR1, ε_o	5%c_{tip}	0.17
AMR2, ε_o	2.5%c_{tip}	0.20
AMR2, $\varepsilon_o/4$	2.5%c_{tip}	0.26
Holst/Pulliam [1]	1.25%c_{tip}	0.22

Table 8 Vortex core growth with wake age. M_{tip}=0.625, θ=14°, and Re=2.1 million.

All OVERFLOW simulations were solved on NASA's Pleiades supercomputer system. The TRAM required 1 wall-hour/rev for the Baseline grid system and 18 wall-hours/rev for the AMR2 grid system. These timings are based on using 1,536 Nehalem 2.93GHz cores.

4.4 UH-60A Rotor in Forward Flight

A brief description of a loosely coupled OVERFLOW/CAMRAD II simulation for a UH-60A rotor in forward flight is now presented to demonstrate the AMR process with flexible rotor blades. Flight Counter C8534, also known as a high-speed case, has M_∞=0.236, M_{tip}=0.64, and an advance ratio μ=0.37. This computation was carried out using 2nd-order time accuracy (Δt=¼°), 5th-order spatial differences, and the SA-DES turbulence model with the SARC correction. There are 40 dual-time subiterations, which gives at least a 2.6-order subiteration drop between time steps. Figure 28 shows a side view of the AMR grids. AMR0 corresponds to a wake grid spacing Δ=10%c_{tip}. Here, AMR is used to automatically detect the rotor wake rather than highly resolve it. This approach has the advantage of not requiring any a priori knowledge of the wake size and position. AMR2 uses a wake grid spacing of Δ=10%, 5%, and 2.5%c_{tip} to highly resolve the rotor wake. Figure 29 shows that the AMR2 wake has much greater detail than the AMR0 wake. The WSL forms a helical path that is convected downward and downwind. Note that the AMR2 vortex cores are much smaller in diameter than the AMR0 system. Fine details of the blade trailing-edge shear layers are clearly seen, and the interaction of these wake shear layers with the vortex cores produces some vortical worms, similar to the TRAM rotor in hover. The

Case	Grid Points (millions)	No. Cores	hr/rev
AMR0	61	1,536	5.4
AMR2	754	3,072	23.8

Table 9 Computer wall-hrs for Flight Counter C8534 using 2.93 GHz Intel Westmere cores.

turbulent eddies shed from the rotor hub are smaller and have greater detail than the coarse-grid result. The trim tab vortices are also evident.

Figure 30 compares the OVERFLOW normal force and pitching moment coefficients as a function of azimuth angle with the flight-test data. The overall comparison is good at all four radial locations. There is no difference in the AMR0 and AMR2 normal force and pitching moment coefficients because there is no BVI. The means are removed in these comparisons, a common practice in rotorcraft code validation due to offset errors that may occur in measurement. The AMR grid size and computer runtimes are listed in Table 9.

Further details and analysis, including LC and time-accuracy convergence are reported in Ref. [6].

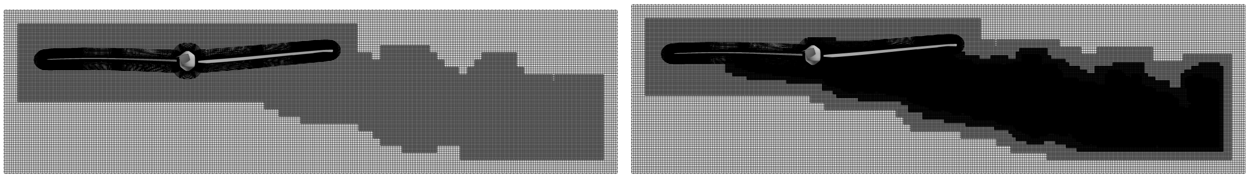

a) AMR0 grid, Δ=10%c_{tip}. b) AMR2 grid, Δ=10%, 5%, and 2.5%c_{tip}.

Figure 28 AMR grids. UH-60A Flight Counter 8534: M_∞=0.236, M_{tip}=0.64, μ=0.37.

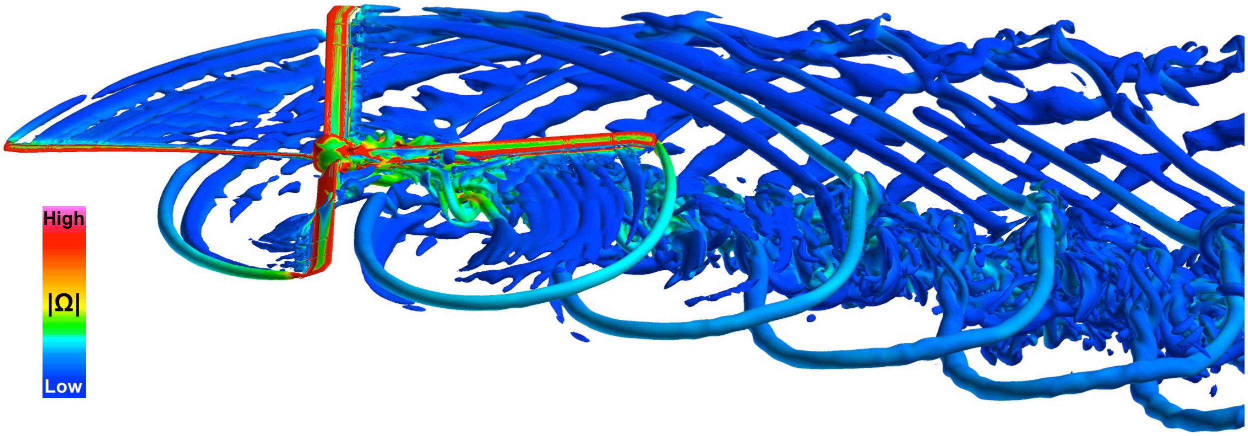

a) AMR0 grid, Δ=10%c_{tip}.

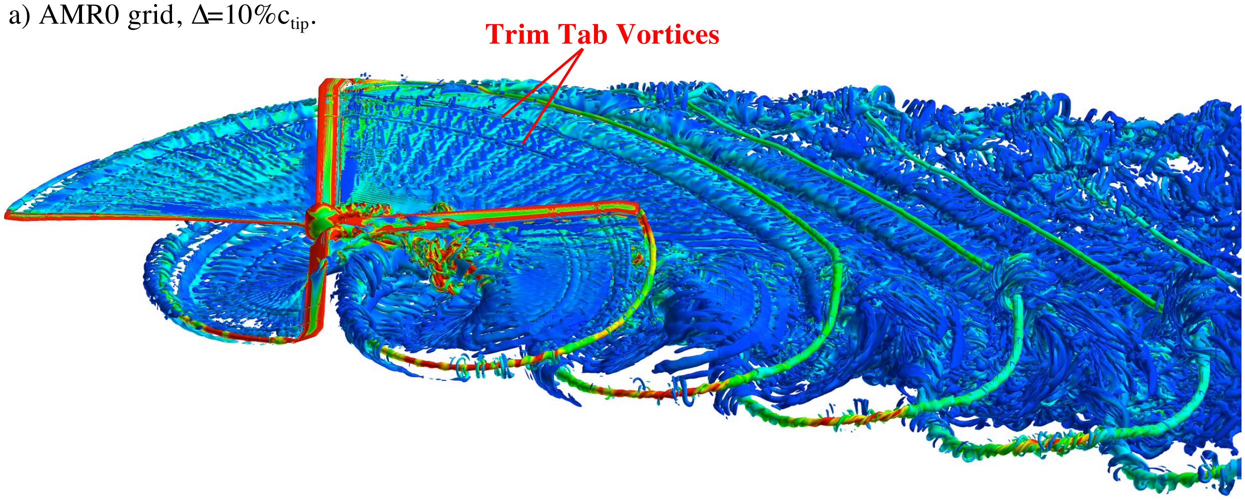

b) AMR2 grid, Δ=10%, 5%, and 2.5%c_{tip}.

Figure 29 AMR vortex wakes. UH-60A Flight Counter 8534: M_∞=0.236, M_{tip}=0.64, μ=0.37.

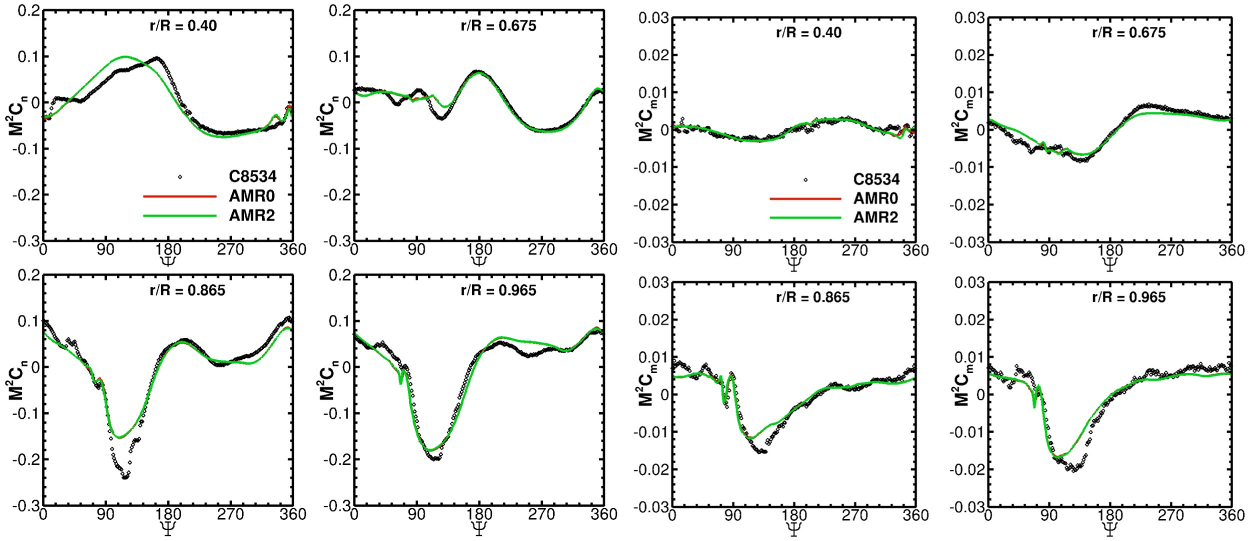

a) Normal force coefficient. b) Pitching moment coefficient.

Figure 30 UH-60A Flight Counter 8534: M_∞=0.236, M_{tip}=0.64, μ=0.37.

5. Conclusions and Future Work

Time-dependent fully-turbulent RANS and DES simulations for the isolated V22 (TRAM) rotor in hover and the isolated UH-60A Blackhawk rotor in forward flight have been carried out with the OVERFLOW Navier-Stokes code. The numerical approach used 2nd-order time accuracy, 5th-order central differencing, and adaptive mesh refinement (AMR). The RANS and DES solutions were based on the Spalart-Allmaras (SA) turbulence model. The following statements pertain to the TRAM rotor in hover.

- The NB rotor-blade grid resolution and spatial accuracy was more important in predicting FM than the grid resolution in the OB grids (rotor wake). In fact, the use of high-order differencing and fine meshes in the wake had no significant effect on the computed FM. It had been previously thought that poor wake-grid resolution was responsible for under-predicting FM.
- SA-DES accurately predicted the FM within experimental error for a collective sweep of $6° \leq \theta \leq 16°$. The SA-RANS model generated excessively large non-physical TEV in the rotor wake. When there was significant BVI, the large TEV was transferred to the rotor blade boundary layers, greatly reducing the predicted FM. The DES turbulent length scale provided a more realistic physics-based length scale in the rotor wake, greatly reducing the TEV. The FM is now predicted within experimental error, even when there is BVI.
- A dynamic AMR process was used to resolve the rotor wake up to 4x finer than a baseline, engineering resolution. Time-dependent flow visualization revealed a complex interaction between the rotor blade TE WSL and the tip vortices. Small turbulent vortical worms formed through a vortex stretching process as the WSLs were entrained into the tip vortices. The computed size of the vortex cores was in good agreement with experiment. A factor of two refinement in the wake, from Δ=5%c_{tip} to 2.5%c_{tip}, only had a small effect on the size of the largest turbulent worms. The accurate prediction of FM and vortex core size, together with experimental evidence suggestive of vortical worms, adds physical credibility to these computed flow structures.

Flow simulations were also carried out with the UH-60A Blackhawk isolated rotor in forward flight.

- AMR successfully found and resolved the rotor tip vortices and wake shear layers up to 4x finer than the baseline wake grid spacing, without any a priori knowledge of the wake position. This avoids the need to manually identify larger regions in the computational domain to insure the capture of the wake.

- The computed time-varying normal force and pitching moments were found to be in good agreement with flight-test data.
- Complex turbulent wakes included the blade TE WSL, trim tab vortices, and the production of turbulent worms, similar to those found in the TRAM computations.

Future work will include UH-60A simulations in forward flight, where BVI and dynamic stall are prevalent, and near-body AMR to improve the prediction accuracy of the rotor blade loads.

References

[1] Holst, T. L., and Pulliam, T. H., “Optimization of Overset Solution Adaptive Grids for Hovering Rotorcraft Flows,” 2010 AHS Specialists Meeting on Aeromechanics, San Francisco, CA, January 2010.

[2] Nichols, R., Tramel, R., and Buning, P., “Solver and Turbulence Model Upgrades to OVERFLOW 2 for Unsteady and High-Speed Flow Applications,” AIAA-2006-2824, June 2006.

[3] Nichols, R., and Buning, P., “User’s Manual for OVERFLOW 2.1,” University of Alabama at Birmingham, Birmingham, AL, 2008.

[4] Spalart, P. R., and Allmaras, S. R., “A One-Equation Turbulence Model for Aerodynamic Flows,” AIAA-92-0439, January 1992.

[5] Chaderjian, N. M., and Buning, P. G., “High Resolution Navier-Stokes Simulation of Rotor Wakes,” Proceedings of the American Helicopter Society 67th Annual Forum, Virginia Beach, VA, May 3-5, 2011.

[6] Chaderjian, N. M., and Ahmad, J. U., “Detached Eddy Simulation of the UH-60 Rotor Wake Using Adaptive Mesh Refinement,” Proceedings of the American Helicopter Society 68th Annual Forum, Fort Worth, TX, May 1-3, 2012.

[7] Swanson, S. M., McCluer, M. S., Yamauchi, G. K., and Swanson, A. A., “Airloads Measurements from a ¼-Scale Tiltrotor Wind Tunnel Test,” 25th European Rotorcraft Forum, Rome, Italy, September 1999.

[8] Johnson, J. L., and Young, L. A., “Tilt Rotor Aeroacoustic Model Project,” Confederation of European Aerospace Societies (CEAS), Forum on Aeroacoustics of Rotorcraft and Propellers, Rome, Italy, June 1999.

[9] Bousman, W. G., and Kufeld, R. M., “UH-60A Airloads Catalog,” NASA TM 2005-212827, Aug. 2005.

[10] Lorber, P. F., Stauter, R. C., and Landgrebe, A. J., “A Comprehensive Hover Test of the Airloads and Airflow of an Extensively Instrumented Model Helicopter Rotor,” Proceedings of the 45th Annual Forum of the American Helicopter Society, Boston, MA, May 1989.

[11] Pulliam, T. H., and Chaussee, D. S., “A Diagonal Form of an Implicit Approximate-Factorization Algorithm,” *Journal of Computational Physics*, Vol. 39, No. 2, 1981, pp. 347-363.

[12] Lee-Rausch, E. M., and Biedron, R. T., “Simulation of an Isolated Tiltrotor in Hover With an Unstructured Overset-Grid RANS Solver,” American Helicopter Society 65th Annual Forum Proceedings, Grapevine, TX, May 27-29, 2009.

[13] Wissink, A. M., Kamkar, S., Pulliam, T. H., Sitaraman, J., and Sankaran, V., “Cartesian Adaptive Mesh Refinement for Rotorcraft Wake Resolution,” AIAA 2010-4554, July 2010.

[14] Pulliam, T. H., “High Order Accurate Finite-Difference Methods: as seen in OVERFLOW,” AIAA-2011-3851, June 2011.

[15] Buning, P. G., and Pulliam, T. H., “Cartesian Off-Body Grid Adaption for Viscous Time-Accurate Flow Simulations,” AIAA-2011-3693, June 2011.

[16] Ramasamy, M., Johnson, B., and Leishman, J. G., “Turbulent Tip Vortex Measurements Using Dual-Plane Digital Particle Image Velocimetry,” Proceedings of the American Helicopter Society 64th Annual Forum, Montréal, Canada, April 29-May 1, 2008.

[17] Gray. R. B., “An Aerodynamic Analysis of a Single-Bladed Rotor in Hovering and Low-Speed Forward Flight as Determined from Smoke Studies of the Vorticity Distribution in the Wake,” Princeton University A.E. Dept. Report No. 356, 1956.

[18] Gray, R. B., “Vortex Modeling for Rotor Aerodynamics,” The 1991 Alexander A. Nikolsky Lecture presented at the American Helicopter Society 47^{th} Annual Forum, Phoenix, AZ, May 1991.

[19] Shur, M. L., Strelets, M. K., Travin, A. K., and Spalart, P. R., “Turbulence Modeling in Rotating and Curved Channels: Assessing the Spalart-Shur Correction,” *AIAA Journal,* Vol. 38, No. 5, May 2000, pp. 784-792.

[20] Smagorinsky, J., “General Circulation Experiments with the Primitive Equations. I. The Basic Experiment,” *Monthly Weather Review*, Vol. 91, No. 3, pp. 99-164.

[21] Spalart, P., Jou, W-H., Strelets, M., and Allmaras, S. “Comments on the Feasibility of LES for Wings and on a Hybrid RANS/LES Approach,” First AFOSR Conference on DNS/LES, August 1997, Greyden Press, Columbus, OH.

[22] Spalart, P. R., Deck, S., Sur, M. L., Squires, K. D., Strelets, M., and Travin, A., “A New Version of Detached-Eddy Simulation, Resistant to Ambiguous Grid Densities,” *Theoretical and Computational Fluid Dynamics (2006)*, Vol. 20, No. 3, pp. 181-195.

[23] Johnson, W., “Rotorcraft Aerodynamic Models for a Comprehensive Analysis,” American Helicopter Society 54th Annual Forum, Washington, D.C., May 1998.

[24] Potsdam, M., Yeo, H., and Johnson, W., “Rotor Airloads Prediction Using Loose Aerodynamic/Structural Coupling,” *Journal of Aircraft*, Vol. 43, No. 3, May-June 2006, pp. 732-742.

[25] Jiang, M., Machiraju, R., and Thompson, D. S., “Detection and Visualization of Vortices,” *Visualization Handbook*, edited by Christopher R. Johnson and Charles D. Hansen, Academic Press, 2004, pp. 287-301.

[26] Kline, S, Cantwell, B., and Robinson, S., “The Physics of Turbulence in the Boundary Layer,” NASA CR 202437, October 1996.

[27] Anderson, W. K., and Bonhaus, D. L., “An Implicit Upwind Algorithm for Computing Turbulent Flows on Unstructured Grids,” *Computers and Fluids*, Vol. 23, No. 1, 1994, pp. 1–22.

[28] Anderson, W. K., Rausch, R. D., and Bonhaus, D. L., “Implicit/Multigrid Algorithms for Incompressible Turbulent Flows on Unstructured Grids,” *Journal of Computational Physics*, Vol. 128, No. 2, 1996, pp. 391– 408.

[29] Nielsen, E. J., “Aerodynamic Design Sensitivities on an Unstructured Mesh Using the Navier-Stokes Equations and a Discrete Adjoint Formulation,” Ph.D. thesis, Virginia Polytechnic Institute and State University, Blacksburg, VA, 1998.

[30] Dacles-Mariani, J., Zilliac, G., Chow, J., and Bradshaw, P., “Numerical/Experimental Study of a Wingtip Vortex in the Near Field,” *AIAA Journal*, Vol. 33, No. 9, September 1995, pp. 1561-1568.

[31] Sankaran, V., Sitaraman, J., Wissink, A., Datta, A., Jayaraman, B., Potsdam, M., Mavriplis, D., Yang, Z., O’Brien, D., Saberi, H., Cheng, R., Hariharan, N., and Strawn, R., “Application of the Helios Computational Platform to Rotorcraft Flowfields,” AIAA-2010-1230, January 2010.

[32] Yamauchi, G. K., NASA Ames Research Center, Moffett Field, CA. Private communication, April 2011.

[33] Leishman, J. G., and Bagai, A., “Challenges in Understanding the Vortex Dynamics of Helicopter Rotor Wakes,” *AIAA Journal*, Vol. 36, July 1998, pp. 1130-1140.

[34] McAlister K., and Heineck, J., “Measurements of the Early Development of Trailing Vorticity From a Rotor,” NASA/TP-2002-211848, AFDD/TR-02-A001, May 2002.

[35] Ramasamy, M., Johnson, B., and Leishman, J. G., "Understanding the Aerodynamic Efficiency of a Hovering Micro-Rotor," *Journal of the American Helicopter Society*, Vol 53, (4), October 2008, pp. 412-428.